University of Stuttgart
Institute of Geodesy

Monitoring inland surface water level from Sentinel-3 data

Master Thesis
Geomatics Engineering
University of Stuttgart

Bo Wang

Stuttgart, February 2019

Supervisors: M.Sc. Omid Elmi
University of Stuttgart

Prof. Dr.-Ing. Nico Sneeuw
University of Stuttgart

Erklärung der Urheberschaft

Ich erkläre hiermit an Eides statt, dass ich die vorliegende Arbeit ohne Hilfe Dritter und ohne Benutzung anderer als der angegebenen Hilfsmittel angefertigt habe; die aus fremden Quellen direkt oder indirekt übernommenen Gedanken sind als solche kenntlich gemacht. Die Arbeit wurde bisher in gleicher oder ähnlicher Form in keiner anderen Prüfungsbehörde vorgelegt und auch noch nicht veröffentlicht.

Ort, Datum

Unterschrift

Abstract

Inland surface water bodies (e.g. lakes and rivers) are very important to the nature and human society. To monitor the water level of inland water bodies, gauge stations were built since 19th century, but the amount of the stations is declining since the 1970s because of lack of maintenance. An accurate and continuous monitoring of lakes and rivers is available because of the satellite altimetry missions launched, e.g. Jason-2 and ENVISAT. These satellites can provide water level with proper spatial and temporal resolution.

In the recent past, researchers have used different satellite mission observations to generate time series of inland water level in order for monitoring the water bodies. In this thesis, we use the new designed satellite mission Sentinel-3, which carries different sensors, to generate the water level time series of Dongting Lake and Poyang Lake in China. Initially, we combine the altimetry measurements with satellite images to determine virtual station. We choose Sentinel-3 Ku band data and on-board Ocean tracker to generate the water level time series. Afterwards, we apply different waveform retracking algorithms (5β-parameter and OCOG) to compare the results with on-board tracker. We also validate the results with the other database, then investigate the waveforms of each sampling date.

The comparisons show the three tracking methods we used are capable to Quasi-Specular waveforms, and OCOG shows the best result to flat patch waveforms. Furthermore, some suggestions for improvements are also discussed in the last chapter.

Key Words: Sentinel-3; Altimetry; Water Level; Waveform Retracking

Contents

List of Figures

List of Tables

Chapter 1

Introduction

1.1 Motivation

Water is the most precious resource in the nature, and fresh water supply is under threat of non-renewability due to the growing demand (Kim et al. 2008). On the earth, the total volume of water is evaluated about 333 million km^3, which includes 97.5% salt water and 2.5% fresh water, and only 0.3% of fresh water is in liquid form on the earth surface, i.e. lakes, reservoirs and rivers (Gleick 1993, Eakins & Sharman 2010).

The inland surface water bodies—water in the lakes, reservoirs, creeks, streams, rivers—are vitally important to our daily life. The main uses of surface water include drinking-water, public use, irrigation use, and industry use by the thermoelectric-power cooling electricity-generating equipment. The majority of water used for thermoelectric power, public supply, irrigation, mining, and industrial purposes came from inland surface water sources (Kenny et al. 2009). However, floods and droughts are extreme hydrologic natural disaster (Cooley 2006). They have a marked impact on fertile soil, supply of fresh water and transportation corridor. These extreme events reflect the probabilities of anthropogenic climate change (Peterson et al. 2008). Moreover, extreme events (i.e. floods and droughts) cause changes in natural and human society much more than ordinary climatic conditions (Peterson et al. 2012). Consequently, continuous monitoring on the surface water bodies is necessary to forecast and analyze the possible hydrological disasters.

In order to manage and monitor the inland water resources, the level of water bodies is of great concern. For this purpose, in-situ networks of gauging stations were built in the past decades, which record the data of discharge of stream and water level with specific time intervals. However, to maintain and build these gauging stations is time-consuming and costly. For political reasons, a large amount of gauging stations which are lack of maintenance in remote areas are abandoned and destroyed by human activities. Figure 1.1 shows that the worldwide number of gauging stations has been decreasing since the 1970s (Fekete & Vörösmarty 2007, Milzow et al. 2011). In addition, processing methods and different seasons have a large impact on the measurement precision. Therefore, for hydrological studies, measuring water level with gauging stations cannot provide satisfied spatial and temporal resolution. Since altimetry satellite missions have been launched, the new technique has been utilized as a reliable and repeatable monitoring method for the ocean and inland surface water bodies, which gives a very large improvement on measurement accuracy and efficiency of monitoring. Water level time series is important not only because it can reflect the change of a water body, but also it has applications shown as follow:

- Estimating river discharge from multi-satellite observations based on measuring the change in total water storage by the Gravity Recovery and Climate Experiment (GRACE) mission (Sneeuw et al. 2014), monitoring the water level using satellite altimetry (Tourian et al. 2013), and extracting river width through satellite imagery (Elmi et al. 2015).

- Estimating lake volume change using water level from satellite altimetry. For example, Tourian et al. (2015) used water level from satellite altimetry and water surface extent from satellite imagery, together with local bathymetry data for computing total water volume in Lake Urmia.

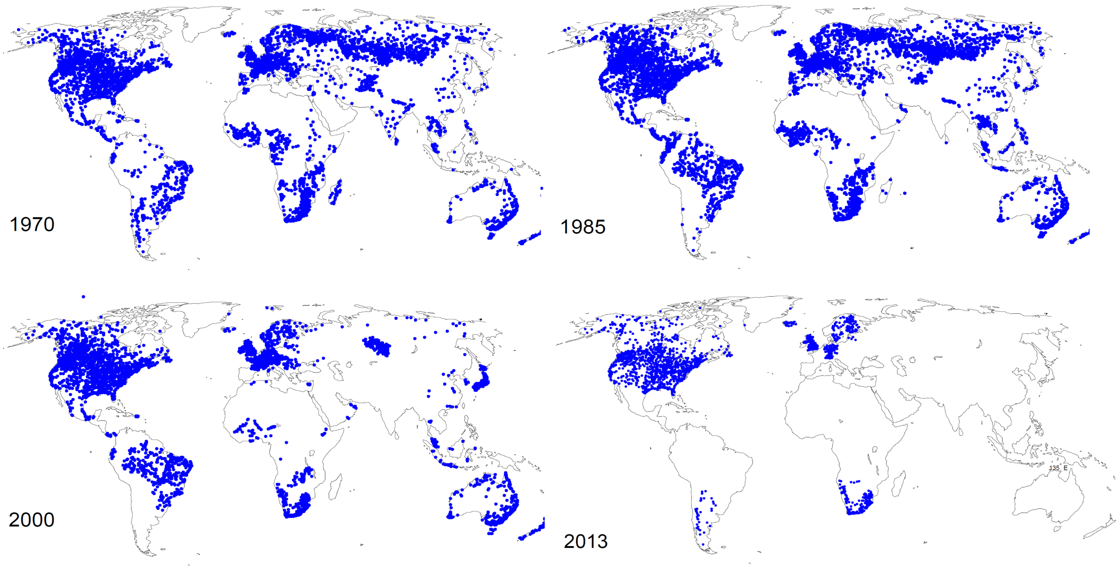

Figure 1.1: *Available stations (updated in March 2017) according to the Global Runoff Data Centre (GRDC) database are depicted for different years (Tourian et al. 2017).*

1.2 Monitoring hydrological cycle by satellite altimetry

Since inland surface water bodies directly effect on the nature and human societies, water protection and disaster forecast increasingly rely on monitoring hydrological cycles. Although, satellite altimeters were designed and optimized for operating over ocean initially (Berry et al. 2005), since decades of studies, altimetry missions also provide an opportunity to monitor inland hydrological cycles (Calmant & Seyler 2006).

After the first earth-orbiting satellite SEASAT launched, the initial work over ocean has been followed by inland water level time series generation (Birkett 1994, Cazenave et al. 1997). Figure 1.2 shows the past, current and future missions, and there are seven satellite altimetry missions currently in service, which are Jason-2, Cryosat-2, HY-2, Saral, Jason-3, ICESat-2 and Sentinel-3. Among these satellite missions, altimeter sensors provide water surface level both in ocean and continent continuously with repeat periods from 10 to 35 days.

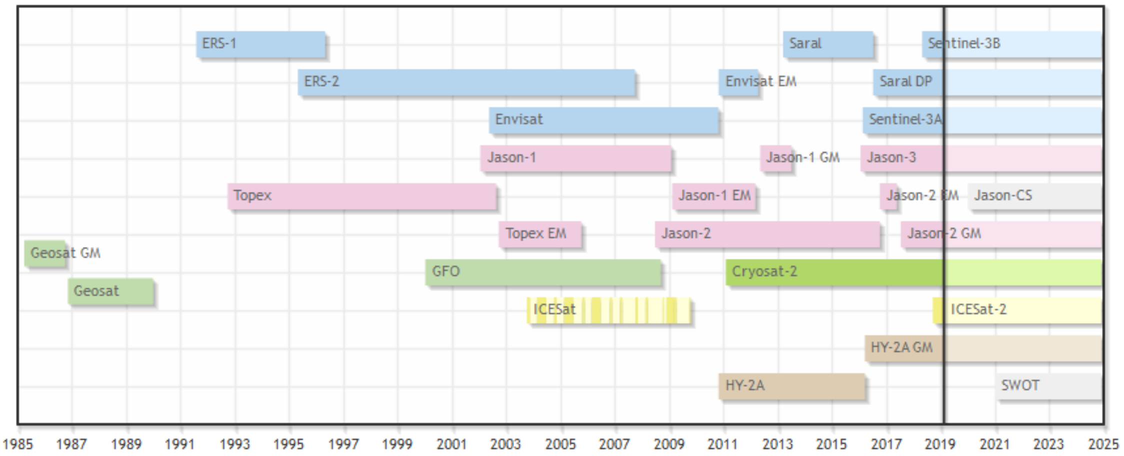

Figure 1.2: *Operating period of satellite altimetry missions (Open Altimeter Database, TUM)*

Due to improvements of measurement accuracy, this enabled researchers to pour attention to studies of inland surface water level monitoring. With development of satellite altimetry missions, the measurement of inland surface water bodies can achieve superior performance in temporal and spatial resolution. Maheu et al. (2003) generated water level time series of the Plata basin (South Africa) with altimetry data from the Topex/Poseidon satellite over the period 1993–2001. They found that all the sites they selected can achieve the precision which is smaller than 0.2 m during the measured period. Berry et al. (2005) applied multiple altimetry missions (TOPEX, ERS-2 and Envisat) to generate water level time series of Amazon basin. They compared the altimetry data with gauge station measurements, as a result, the Pearson correlation coefficient for TOPEX, ERS-2 and Envisat according to gauge station are 0.91, 0.93 and 0.98, respectively. For comparison between the data from altimetry satellite missions and in-situ gauging stations, Crétaux & Birkett (2006) studied 10 lakes in central Asia, they found the accuracy of satellite altimetry is homogeneous, which depends on the amount of satellite data. Crétaux et al. (2011) took advantage of Jason-1 data and in-situ gauging records, for the Lake Victoria, they presented the water level comparison with the RMS (Root Mean Square) of 2.6 cm and the correlation coefficient is 0.99. Results indicate that the altimetry provides extremely accurate water level in the continuous monitoring series. Schwatke et al. (2015) presented a new approach to generate water level time series using multi-mission altimetry satellites. This method is concerning data processing, Kalman filter and meticulous outlier detection. In their cases, the generated RMS with respect to in-situ data from 4 to 36 cm for lakes and 8 to 114 cm for rivers. In the monitoring of the Inner Niger Delta, Normandin et al. (2018) selected data from 19 gauge stations from 1995 to 2017 to compare with the past and current missions. Results imply that 80% of the cases can get correlation coefficient larger than 0.8 and the RMSE smaller than 40 cm in 48% of cases. They verified that the recently launched missions (SARAL, Jason-3 and Sentinel-3A) performed better than the past missions, especially the use of the Ka-band for SARAL and the Synthetic Aperture Radar (SAR) mode for Sentinel-3A.

Over the past few years, several research teams have already established hydrological databases of inland surface water level time series derived from satellite altimetry missions (e.g. DAHITI, HydroSat and Hydroweb). However, results of researches on different inland surface water bodies indicate that large lakes and wide rivers normally provide better performances than that of small lakes and narrow rivers. This is caused by disturbances of lands, rough water surfaces and lag effects of the Automatic Volume Control (AVC) when altimetry waveforms generated while it measures the shores of rivers or lakes (Guo et al. 2009). Consequently, contaminated waveforms should be retracked to those effects. In addition, numerous elements can also affect the accuracy of the measurements from altimetry satellite missions. Among these errors, some come from the altimeter, some are from the other on-board instruments, moreover, the microwave propagation errors in the atmosphere and geophysical adjustments also should be considered.

1.3 Objectives

In this thesis, we take advantage of Sentinel-3A SAR Radar Altimeter (SRAL) data to monitor the variation of the water level of Dongting Lake and Poyang Lake. As the Sentinel-3A satellite mission was launched on 16 February 2016, hence the data are available in these areas since June 2016. The objectives in this thesis are shown as follow:

- Select the virtual station of the lake to generate the water level time series with the on-board retracked altimeter range.
- Implement different retraking algorithms to analyze the different results.
- Compare the water level variation with that of the other database.
- Combine the altimeter measurement positions in the tracks with optical remote sensing images of near synchronous acquisition dates in different seasons.
- Analyze the performances of waveforms in different seasons.

1.4 Structure of this thesis

The structure of this thesis to implement the objectives is divided into the following chapters. In Chapter 2, the detailed principle of satellite radar altimetry will be presented. Furthermore, Sentinel-3 mission and potential challenges will also be introduced in this chapter. In Chapter 3, waveform structure and different retracking algorithms will be explained in more details. For Chapter 4 and 5, these two chapters present our implementations of two lakes, and we will analyze the results in this part. Chapter 6 indicates the summary, conclusion and further research direction.

Chapter 2

Satellite altimetry measurement

Altimetry satellites are basically used to determine the distance between the altimeter and a target surface on the earth, which measure the round-trip time of radar pulse (Chelton et al. 2001, Deng 2003). The magnitude and shape of radar pulse echoes (waveforms) contain the information about the characteristics of the surface which caused the reflection (Łyszkowicz & Bernatowicz 2017). For the ocean monitoring, altimeters can normally obtain best results because of spatial homogeneity of the ocean surface. Recent satellite altimetry missions can achieve the accuracy of measurements up to 5 cm over the ocean (Shum et al. 1998). For surfaces, which are not homogeneous with discontinuities or significant slopes (e.g. ice sheets, rivers, lakes and land surfaces), to obtain accurate interpretation is more arduous.

2.1 Measuring principle

2.1.1 Range measurement

There are three main parts of a satellite altimeter, including a radar signal transmitter (isotropic antenna), a receiver and an on-board extremely stable oscillator (Ghosh et al. 2017). The signal transmitter emits microwave signals at high frequency (over 1 700 pulses/second) to the earth, and the receiver receives the echoes from the earth surface. If a precise measurement of round-trip time between the altimeter and the water surface is recorded, the one-way distance called range R can be determined (Fu & Cazenave 2000). Figure 2.1 presents the range measurement from the satellite altimeter to the water surface.

The original range $\hat{R}$ between the altimeter and the water surface is determined by eq. (2.1):

$$\hat{R} = \frac{1}{2}ct\,, \tag{2.1}$$

in which, c is the speed of light, and t is the round-trip traveled time between the altimeter and the water surface.

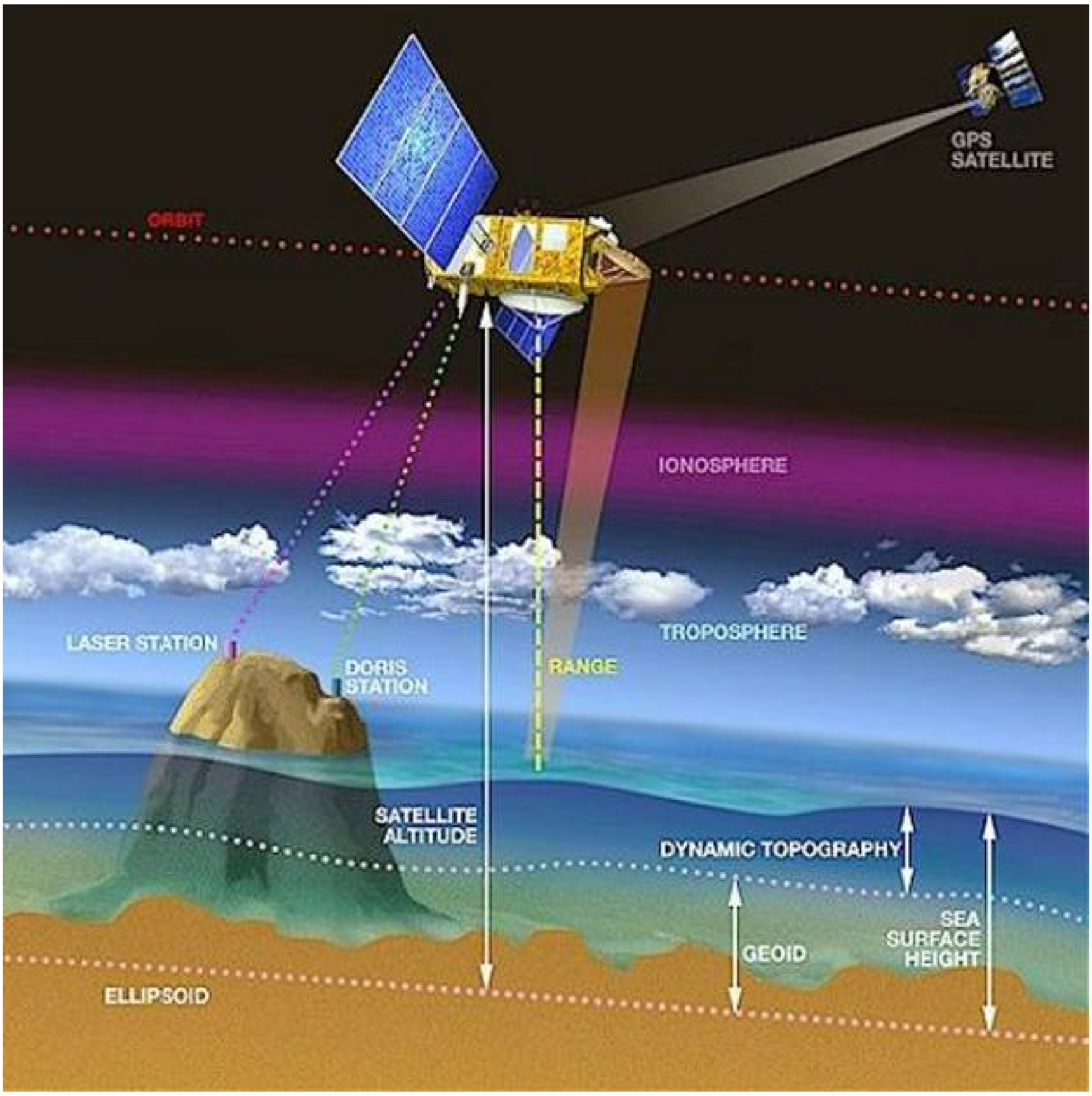

Figure 2.1: *Schematic of satellite altimetry measurement principle (Aviso, 2018)*

It is obvious that the precision of the range depends on the precision of time measurement. If the precision of travel time can be improved to the magnitude of 10^{-11} s, then knowing the speed of light, the resolution of the range measurement can achieve to the magnitude of centimeter (Siddique-E-Akbor et al. 2011). For the part of time correction, it will be introduced in Chapter 3.

Furthermore, there are also some correction parameters ($\triangle R_i$) should be removed from the original measured range, which are caused by pulses propagation in atmosphere, geophysical disturbances and instrumental errors (Dumont et al. 2009). The effects of correction parameters will be introduced in Section 2.2.

Actually, the corrected range R should be presented as eq. (2.2):

$$R = \hat{R} - \sum_i \triangle R_i \tag{2.2}$$

2.1.2 Sea Surface Height

The sea surface height (SSH), is the distance h at a given instant from the water surface to a reference ellipsoid (e.g. WGS84 or Geoid), which is calculated by applying the following equation:

$$\begin{aligned} h &= H_{\text{sat}} - R \\ &= H_{\text{sat}} - \hat{R} + \sum_i \triangle R_i \,, \end{aligned} \tag{2.3}$$

In eq. (2.3), H_{sat} is the altitude of the satellite with respect to the reference ellipsoid derived from the orbital parameters of the satellite. To determine the high precision orbital parameters, the modern altimetry satellite missions carry several sensors, such as Satellite Laser Ranging (SLR), Doppler Orbitography and Radiopositioning Integrated by Satellite (DORIS) and Global Positioning System (GPS) (Pandey et al. 2014).

2.2 Correction parameters

Since the speed of light is a constant during propagation in a vacuum, the range between the satellite and the water surface could be easily determined. However, radar signals slow down because of dry gases, water vapour, and liquid water in the lower atmosphere and electrons present in the upper atmosphere. These effective factors may lead to an error in the range measurement. Hence, geophysical corrections (i.e. inverse barometer, sea state bias, polar tide, ocean tide, earth tide, ionospheric correction, dry tropospheric correction, and wet tropospheric correction) and instrument error corrections (i.e. Doppler correction, time delay due to flight and time delay due to ground corrections and antenna center of gravity) should be removed from the original measured range to get the correct range. Figure 2.2 presents the correction parameters of radar altimetry. We will introduce the main three correction parameters for range estimation in the following subsections.

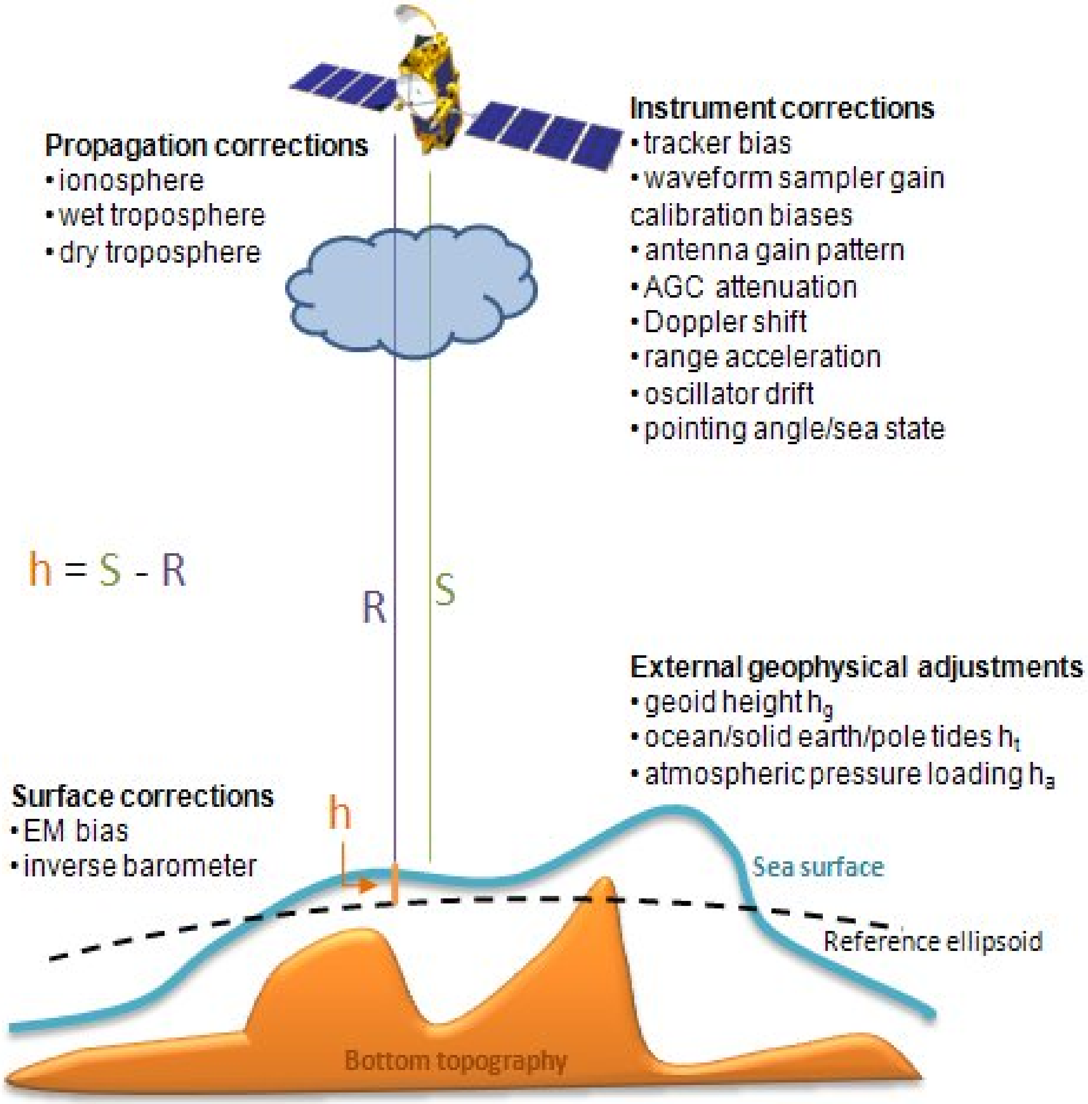

Figure 2.2: Schematic of correction parameters for radar altimetry (CNES)

2.2.1 Dry tropospheric correction

Among all the influence factors making time delay, the dry tropospheric correction (DTC) has the largest range correction due to the dry gas component of the atmosphere (Fernandes et al. 2014). The DTC can be estimated with an accuracy of a few millimeters from surface atmospheric pressure p_s using the modified

Saastamoinen model (Davis et al. 1985), because it is almost linear height dependence with an absolute value of about 2.3 m at sea level and a range of about 0.2 m. The model is described as eq. (2.4):

$$\triangle C_{\mathrm{dtc}} = -\frac{0.0022768\, p_s}{1 - 0.00266\, \cos 2\phi - 0.28 \cdot 10^{-6}\, h_s}\,, \tag{2.4}$$

where p_s is the surface pressure in hPa, ϕ is the geodetic latitude, h_s is the surface height above the geoid (in meters) and $\triangle C_{\mathrm{dtc}}$ results in meters.

In the eq. (2.4), p_s is the total atmospheric pressure, i.e. the partial pressure of dry air and the pressure due to water vapor, this expression actually gives the zenith path delay caused by the hydrostatic component of air and not just by the dry component of atmospheric pressure. The most common sources of atmospheric pressure are the atmospheric models from the European Centre for Medium-Range Weather Forecasts (ECMWF) (Miller et al. 2010), and the National Centers for Environmental Prediction (NCEP).

2.2.2 Wet tropospheric correction

The path delay caused by water vapour, the wet tropospheric correction (WTC), which is one of the major errors during propagation of radar signals in the atmosphere. The most accurate method for modelling this effect is through the measurements of microwave radiometers (MWR) on-board the altimetric missions, because of the high variability over the ocean both in time and space. The passive MWR on-board altimeter satellites retrieve the water vapour percentage from the instantaneous measured brightness temperatures, at the nadir, in channels inside and outside the water vapor absorption line at 22.235 GHz (Scharroo et al. 2004).

From this algorithm, the WTC can be determined by the total column water vapour (TCWV) and near-surface air temperature (T_0) (Bevis et al. 1992). The equation is described as follow:

$$\triangle C_{\mathrm{wtc}}(h_s) = -\left(0.101995 + \frac{1,725.55}{T_m}\right)\frac{\mathrm{TCWV}}{1\,000} \quad , \tag{2.5}$$

where T_m is the mean temperature of the troposphere, which can be modeled from T_0, according to the article of Mendes et al. (2000):

$$T_m = 50.440 + 0.789\, T_0 \quad , \tag{2.6}$$

eq. (2.5) and eq. (2.6) provide the WTC at the level of the atmospheric model orography. The height dependence of water vapor is not easy to model, due to its large variability. In spite of this, Kouba (2008) proposed the following empirical expression:

$$\triangle C_{\mathrm{wtc}}(h_s) = \triangle R_{\mathrm{wtc}}(h_0)\, e^{\frac{h_0 - h_s}{2000}} \quad , \tag{2.7}$$

in which, h_s and h_0 are the ellipsoidal heights of the model orography and surface, respectively.

2.2.3 Ionospheric correction

The refraction caused by electrically-charged particles in the atmosphere has to be taken into account, which is a part of range estimation for satellite altimetry. Most of those charged particles occur in ionosphere, the part of the atmosphere between an altitude of 50 and 2 000 km, where ions are produced by the photoionization of atomic and molecular gasses (Rush 1986).

The total delay affecting the radar pulse along its path through the ionosphere, $\triangle C_{\mathrm{ion}}$, can be estimated from the integral over height of the ionospheric refractivity $N_{\mathrm{ion}}(z)$, which is in turn proportional to the electrons in the ionosphere, $n_e(z)$. Moreover, the ionospheric refraction is dependent on frequency f, which is inversely proportional to the square of the frequency (Chelton et al. 2001):

$$\begin{aligned} \triangle C_{\mathrm{ion}}(f) &= 10^{-6} \int_0^R N_{\mathrm{ion}}(z)\, dz \\ &= \frac{k}{f^2} \int_0^R n_e(z)\, dz \quad , \end{aligned} \tag{2.8}$$

where $k = 40.250\, m^3 \cdot Hz^2 \cdot electrons^{-1}$, n_e is expressed in electrons/m^3, f in Hz and $\triangle R_{\mathrm{ion}}$ results in meters. The last integral in eq. (2.8) represents the atmospheric columnar electron density. This total electron content (TEC) is usually expressed in TECU (TEC units), with 1 TECU = 10^{16} electrons/m^2, allowing the altimetric ionospheric path delay to be more practically written as:

$$\triangle C_{\mathrm{ion}}(f) = \frac{\mathrm{kTEC_{alt}}}{f^2} \quad , \tag{2.9}$$

where $k = 0.40250\,m \cdot \mathrm{GHz}^2 \cdot \mathrm{TECU}^1$, f is expressed in GHz, and $\mathrm{TEC}_{\mathrm{alt}}$ is the total electron content below the altimeter. For altimeters operating in the Ku-band (approximately 13.6 GHz), this comes out to 2.18 mm of path delay per TECU (Schreiner et al. 1997). Operating on two different frequencies, recent high-precision radar altimeters flying on Envisat, Jason-1, Jason-2 and TOPEX, in principle, direct estimation of TEC_{alt} from the difference between the measured ranges on the two frequencies (Scharroo & Smith 2010):

$$\mathrm{TEC}_{\mathrm{alt}} = \frac{f_{\mathrm{Ku}}^2\, f_{\mathrm{C,S}}^2}{f_{\mathrm{Ku}}^2 - f_{\mathrm{C,S}}^2}\,\frac{R_{\mathrm{C}} - R_{\mathrm{Ku}}}{k} \quad . \tag{2.10}$$

The ranges, R_{Ku} and $R_{\mathrm{C,S}}$, in eq. (2.10) are those measured on the primary Ku-band and on the secondary C-band (5.3 GHz for TOPEX and Jason) or S-band (3.2 GHz for Envisat), respectively. GNSS is used for deriving TEC to estimate the ionospheric correction for altimeter range measurement, additionally, the necessary interpolation in space and time to the altimeter ground track, altitude scaling has to be performed (Iijima et al. 1999).

2.3 Satellite altimetry missions

Since the first oceanographic satellite SeaSat launched in 1978, different missions have been providing vital monitoring technique for the surface water bodies. These satellite altimetry missions with precise orbit determination continuously measure the water level on the earth, including oceans, lakes and rivers.

2.3.1 Sentinel-3 mission

Sentinel-3A was launched on 16th February in 2016, which is jointly operated by European Space Agency (ESA) and European Organisation for the Exploitation of Meteorological Satellites (EUMETSAT) to deliver operational ocean and land observation services. The main objective of the Sentinel-3 mission is to measure sea surface topography, sea and land surface temperature, and ocean and land surface colour with high accuracy and reliability to support ocean forecasting systems, environmental monitoring and climate monitoring. It carries different instruments, which are Ocean and Land Colour Instrument (OLCI), Sea and Land

Surface Temperature Instrument (SLSTR), SAR Radar Altimeter (SRAL), and Microwave Radiometer (MWR). Figure 2.3 shows the main instruments of Sentinel-3.

SRAL is the instrument providing the measured range and corrections, which we use for generating the inland surface water level time series in this thesis. The main frequency used for range measurements is the Ku-band (13.575 GHz, bandwidth 350 MHz), however, contrary to Cryosat, a second frequency is used. The C-band frequency (5.41 GHz, bandwidth 320 MHz) is used for ionospheric correction. There are two radar modes of SRAL, one is Synthetic Aperture Radar (SAR) mode, and the other one is Low-Resolution Mode (LRM). The SRAL instrument is always operated at High Resolution Mode (i.e. SAR mode), and Low Resolution Mode (LRM) is for back-up only.

OLCI is a medium-resolution imaging spectrometer that uses five cameras to provide a wide field of view. OLCI has 21 spectral bands with wavelengths ranging from the optical to the near infrared. Bands vary in width from 2.5 nm to 40 nm, and serve a variety of different purposes, including measuring water vapor absorption, aerosol levels, and chlorophyll absorption. OLCI products are available at two spatial resolutions: full resolution at approximately 300 m and reduced resolution at approximately 1.2 km.

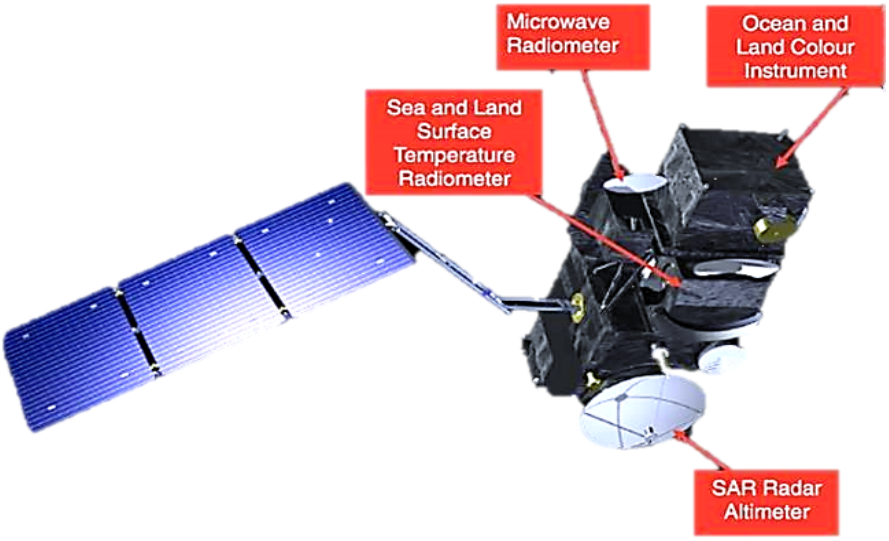

Figure 2.3: *Main on-board instruments of Sentinel-3 (Credit: ESA)*

Sentinel-3 is equipped with a new-generation (multi-channel and digital) receiver, which is able to track up to seven beacons simultaneously. Ricker et al. (2012) indicated that real-time accuracy of the DORIS navigation solution (Diode) is about 3.5 cm. Diode is used to drive the open loop tracking mechanism of the SRAL altimeter. The combination of both GPS and DORIS measurements in Precise Orbit Determination (POD) processing improves the final performance on the three directions, with the precision can be up to 1 cm (Kang et al. 2006).

2.3.2 Other satellite altimetry missions

Except Sentinel-3A, there are 6 other satellite altimetry missions currently operating in the space. Satellites Jason-2 and Jason-3 with a relatively short repeat cycle (10 days), able to observe the same spot on the ocean frequently but with relatively widely-spaced ground tracks (315 kilometres at the equator). Satellite SARAL with a 35-day repeat cycle, is on the same ground-track as ERS-1 & 2 and Envisat. Cryosat-2 ables to work with an interferometric mode, with a high orbit inclination of 92° to satisfy the scientific requirements for observing the poles and the ice sheets. HY-2A operates in the first period (initially planned over the first 2 years) with a 14-day cycle (altitude 971 km), then in a second period (initially planned to last one year) with geodetic orbit (168-day cycle, altitude 973 km). Table 2.1 gives the specifications and instrument characteristics for different satellite altimetry missions.

Table 2.1: Parameters of different altimeter missions (AVISO, 2018)

Altimeter	Revisit Time	Altitude [km]	Band	Antenna Beamwidth[°]	PRF [Hz]	Waveform Gates	Nominal Tracking Point	Pulse Width [ns]
SEASAT	17 days	800	Ku	1.59	1020	60	29.5	3.125
GEOSAT	17 days	800	Ku	2.00	1020	60	30.5	3.125
ERS-1	35 days	785	Ku	1.30	1020	64	32.5	3.030
TOPEX	10 days	1336	Ku	1.10	4500	128	32.5	3.125
			C	2.70	1200	128	32.5	3.125
Poseidon	10 days	1336	Ku	1.10	1700	60	29.5	3.125
ERS-2	35 days	785	Ku	1.30	1020	64	32.5	3.030
GFO	17 days	880	Ku	1.60	1020	128	32.5	3.125
Jason-1	10 days	1336	Ku	1.28	1800	104	31.0	3.125
			C	3.40	300	104	31.0	3.125
Envisat	35 days	800	Ku	1.29	1800	128	46.5	3.125
			S	5.50	450	64	25.5	6.250
ICESat-1	90 days	600	Laser	0.029	40	1000	500	5.000
			Laser	0.010	40	544	272	5.000
Jason-2	9.9 days	1336	Ku	1.26	1800	104	31.0	3.125
			C	3.38	300	104	31.0	3.125
Cryosat-2	369 days	717	Ku	1.08,1.20	18181	128	63.0	1.5625
SARAL	35 days	800	Ka	1.29	1800	128	46.5	3.125
Jason-3	9.9 days	1336	Ku	1.28	1800	104	31.0	3.125
			C	3.40	300	104	31.0	3.125
Sentinel-3A	27 days	814.5	Ku	1.28	1924	128	44.0	3.125
			C	3.40	274.8	128	44.0	3.125

Chapter 3

Altimetry waveform

3.1 Waveform construction

A satellite altimeter emits short radar pulses towards the earth surface in the nadir direction and measures the reflected echoes. Microwave energy from a single radar pulse radiating within a thin, spherical shell away from the nadir antenna interacts with the earth's surface. When the wavefront encounters the nearest water surface, it illuminates one point and a reflected echo begins to return to the altimeter. The reflected signal intensity grows through the area of interaction between pulse and surface increasing. Thereafter, the backscattered energy begins to decline due to the finite antenna beamwidth and fewer reflected facets in off-nadir directions. The power of the reflected signal is recorded within the duration of the pulse, which construct the initial waveform. The procedure of waveform construction is shown in Figure 3.1.

Normally, a waveform contains noises, which are from the reflected signals. To reduce the noise in waveforms, the reflected pulses are averaged and construct a mean waveform. The averaged returned waveform known as Brown model, is the mean of returned power series recorded by the satellite altimeter, and it contains mainly of three parts (Brown 1977) (Figure 3.2):

- **The thermal noise:** The altimeter sometimes generates the noise power before the first return of a signal from the scattering surfaces. It performs a constant power level to the return waveform.
- **The leading edge:** It is the main part of a waveform which records the rising procedure of return power from the scattering surfaces. From this part, the information about the range between the satellite altimeter and the mean sea surface at the nadir can be extracted.

- **The trailing edge:** This part is constructed as the return power from the scattering surface decaying. It can be approximated by a straight line whose slope depends on the altimeter antenna pattern and the off-nadir angle (Chelton et al. 2001).

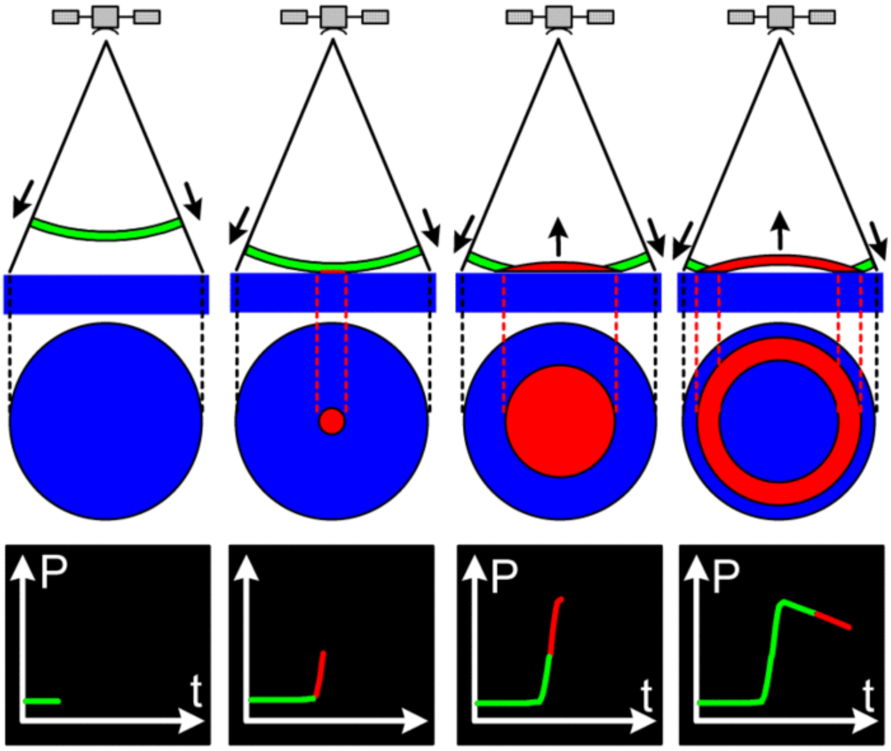

Figure 3.1: The procedure of constructing the returned waveform (Credit: CNES)

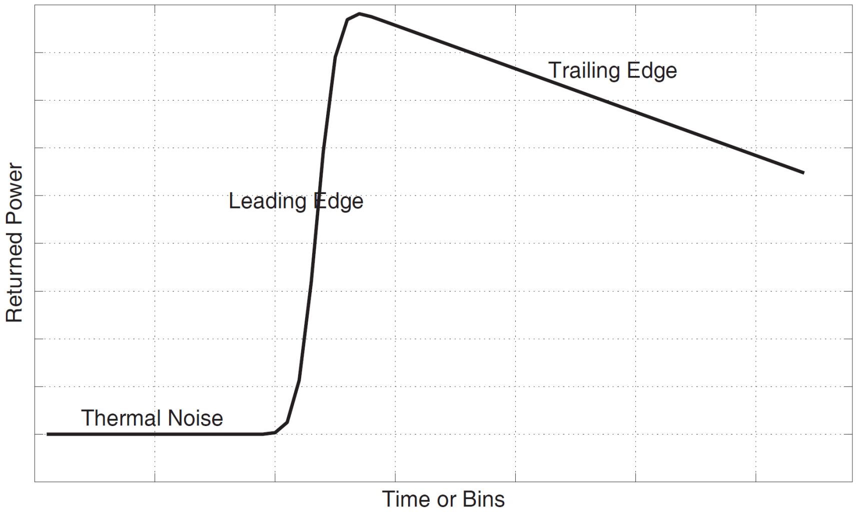

Figure 3.2: Schematic altimeter mean return waveform over ocean surface (Tourian 2012)

The waveform indicates the reflectivity (estimated from the amount of power in the reflected pulse) and the large-scale roughness of the scattering surface. The on-board tracker is an algorithm on board the satellite which computes the range to the nadir by recording the round trip time of the pulse. This travel time represents the time that the mid-point of the radar pulse needs to return from target surface at nadir. Hence, the on-board tracker calculates the time by finding the mid-point on the leading edge. The on-board tracker continuously adjusting the range window and try to keep the leading edge of the waveform stable at the fixed centre of the range window, which is known as tracking gate (Deng 2003). The tracking gate is a pre-designed bin index of a waveform, which defines the initial range between the satellite and the surface at nadir. Therefore, on-board tracker itself will find out the half-power point of the leading edge and determine the offset to the tracking gate. The offset represents the range correction, and the tracked range can be calculated.

3.2 Waveform types

Over the ocean, normally the altimeter can receive Quasi-Brown returned waveforms with a sharp and stable narrow peak (Berry et al. 2005). Over inland water, the waveform is complicated and normally contaminated by the slope, roughness and vegitation cover within the footprint. Waveforms from large lakes and wetlands are the typical high powered spikes which are similar to returned signals from oceans (Birkett 1995). A waveform becomes broader and more noisy as samples of the waveform are contaminated by non-water bodies. Due to the inhomogeneous surface within the large footprints of radar, the number of Quasi-Brown model waveforms decreases and more narrowly peaked waveforms appear by decreasing the size of water body (Berry et al. 2005). In other words, waveforms over inland water bodies do not show similar patterns, which are normally classified into four types: Quasi-Brown model, flat patch, Quasi-Specular and multiple peak waveforms (Guzkowska et al. 1990), shown as Figure 3.3.

The Quasi-Brown waveforms are characterized by the sharp leading edge with a wide slowly decreasing trailing edge. This kind of waveform is normally produced over the ocean, large lakes or wide rivers. The Quasi-Specular waveforms have the sharp vertical leading edge and the rapid decrease of trailing edge. This kind of waveform usually produced over narrow rivers. Comparing to Quasi-Specular model, the flat patch waveforms have similar leading edge, but the trailing edge decreases slowly. This kind of waveforms are produced over the water bodies surrounded by low reflecting surfaces. The multiple peak type has double or several peaks in one waveform, which is usually formed over the close to the banks of water bodies.

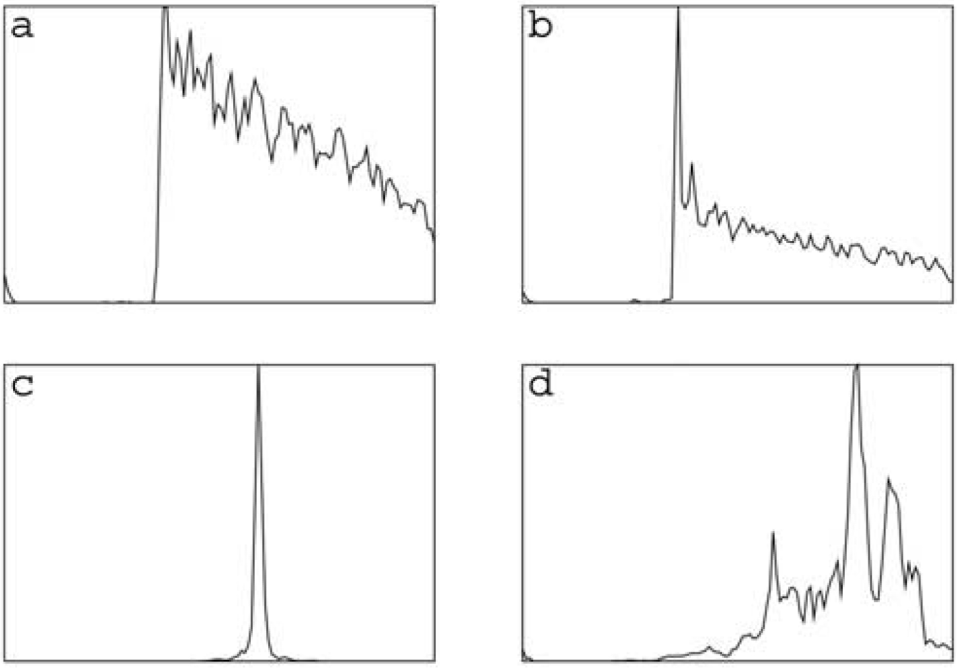

Figure 3.3: *Examples of (a) Quasi-Brown model, (b) flat patch, (c) Quasi-Specular and (d) multiple peak over inland water (Berry et al. 2005)*

3.3 Hooking effect

As a satellite altimeter measures the range in the nadir direction, the footprint location is supposed to be directly under the altimeter. Since the water surface reflects usually more strongly than the surrounding land surface, the altimeter measures the distance to the water surface even when it is not nadir-positioned over the water. The off-nadir distortion of altimetry measurements is known as hooking effect. This issue usually occurs that the water surface with high reflected power is at the edge rather than at the nadir of the radar footprint. Figure 3.4 demonstrates the measured off-nadir distances form a parabolic shape in the along-track altimetric height profiles (Da Silva et al. 2010).

The satellite altimeter along the orbit measures the water body with the range ρ_i, and the altitude of the satellite is a_i, then the calculated water level is $H_i = a_i - \rho_i$.

However, the actual nadir range between the altimeter and the water surface is ρ_0, and the altitude of the satellite at the zenith of the water body is a_0. Obviously, the true water level should be $H_0 = a_0 - \rho_0$.

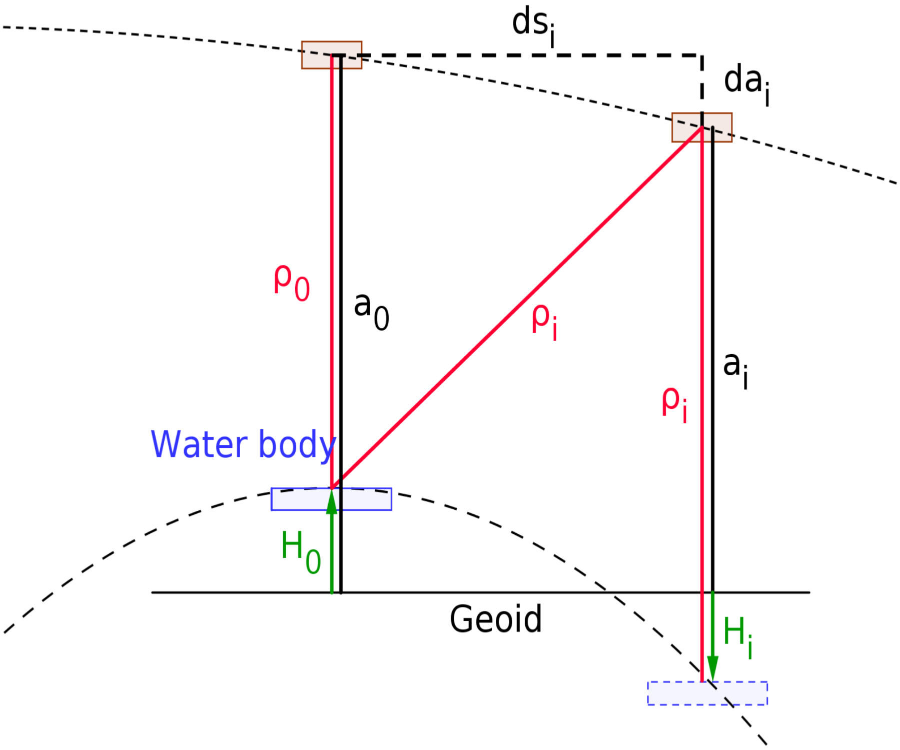

Figure 3.4: *Off-nadir measurement of the slant distance to the water body (Boergens et al. 2016)*

Generally, measurements along the track over water-land transitions always generate hooking effect, shown as Figure 3.5. The left view Figure 3.5(a) is the RGB image with along-track measurements, and the blue dots are the epochs over the water in nadir direction. Figure 3.5(b) shows the peaks of waveforms appear in different bins according to the leading edges have shifts among the measurements. The on-board tracking procedure will then determine the range by fitting this reflected power that traversed a skewed path. Since the range estimation assumes the target is at the satellite nadir, this leads to an overestimated range, i.e., to an underestimated height of the reflecting water surface.

However, the hooking effect can usually be ignored in water level generation if the water body is large which has enough nadir-positioned measurements. For narrow rivers or small lakes, the off-nadir measurements should be used to generate the water level by averaging even better than the solo measurement over the water body.

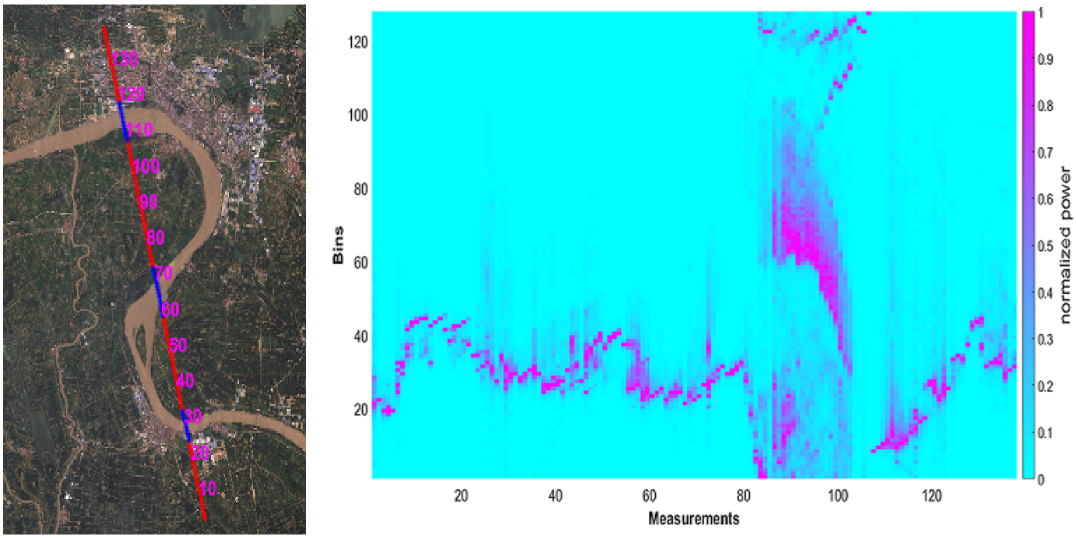

(a) *Measurements along-track over Yangtze River*

(b) *Power of waveforms along-track*

Figure 3.5: *Example of the hooking effect from Sentinel-3A altimetry data*

3.4 Waveform retracking

Retracking is a post-processing and analysis of radar altimeter waveform data to retrieve an optimized gate or bin for the range measurement. The main purpose of waveform retracking is correcting the estimated range from on-board tracker. As mentioned above, waveforms over water bodies do not show the same pattern, and the on-board estimation algorithm may be not proper to a specified type of waveform. The on-board tracker continuously computes the mid-point of the leading edge in a limited time, which always leads to a computational error. Near lake shoreline or over shallow water the altimetry waveforms generally contaminated by responses from non-water bodies inside the footprint of the radar. Due to these reasons, retracking is a necessary procedure to improve the quality of range measurements.

As described before, the offset between the retracking gate and the tracking gate presents the error in range measurement (Figure 3.6). The offset can be transformed to range by eq. (3.1):

$$\triangle R_{\text{ret}} = (\text{Gate}_{\text{ret}} - \text{Gate}_{\text{nom}}) \cdot \tau \cdot \frac{\text{c}}{2}\,, \tag{3.1}$$

where $\mathrm{Gate}_{\mathrm{ret}}$ is the retracking gate and $\mathrm{Gate}_{\mathrm{nom}}$ is nominal tracking gate. The parameter τ is sampling rate of the pulse (for Sentinel-3, it is 3.125 ns).

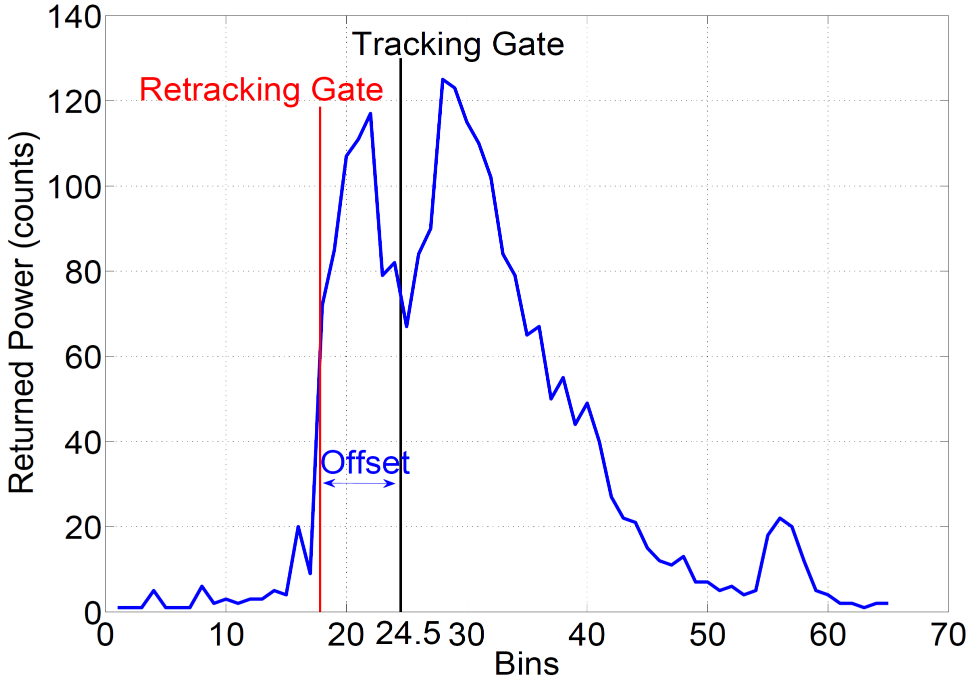

Figure 3.6: *Schematic of retracking (Tourian 2013)*

Although several retracking algorithms are applicable as a post-processing step, the quality of range estimation depends on the type of retracking algorithms. Moreover, there is no single algorithm which can meet the diverse needs of all the waveforms (Lee et al. 2010, Uebbing et al. 2015). Consequently, several retraking algorithms were developed for different type of waveforms, including β-parameter retracker, ocean retracker, Ice-2 retraker and OCOG retracker. Over inland water bodies, the waveform normally contains a narrow peak due to the small size of water. From large amount of researches, β-parameter and OCOG retrackers are always applicable for lakes or rivers. Therefore, for our study these two retrackers will be introduced in the following subsections.

3.4.1 β-parameter retracker

The β-parameter was developed by Martin et al. (1983) to process the waveforms over continental ice sheets, which was firstly used for SEASAT radar altimeter. 5β-parameter function is used to fit the single-ramp returned waveforms, and the 9β-parameter function is used to fit the two-ramp returned waveforms.

The general function of 5β-parameter for retracking the waveform is given as (Martin et al. 1983):

$$y(t) = \beta_1 + \beta_2(1 + \beta_5 Q)P\left(\frac{t-\beta_3}{\beta_4}\right) \tag{3.2}$$

$$Q = \begin{cases} 0 & for \quad t < \beta_3 + 0.5\beta_4 \\ t - (\beta_3 + 0.5\beta_4) & for \quad t > \beta_3 + 0.5\beta_4 \end{cases} \tag{3.3}$$

$$P(x) = \int_{-\infty}^{x} \frac{1}{\sqrt{2\pi}} exp\left(\frac{-q^2}{2}\right) dq \tag{3.4}$$

The model parameters mentioned in Figure 3.7 are:

- β_1: The thermal noise level of the waveform
- β_2: The return signal amplitude
- β_3: The mid-point of the leading edge of the waveform
- β_4: The return waveform rise time
- β_5: The slope of the trailing edge

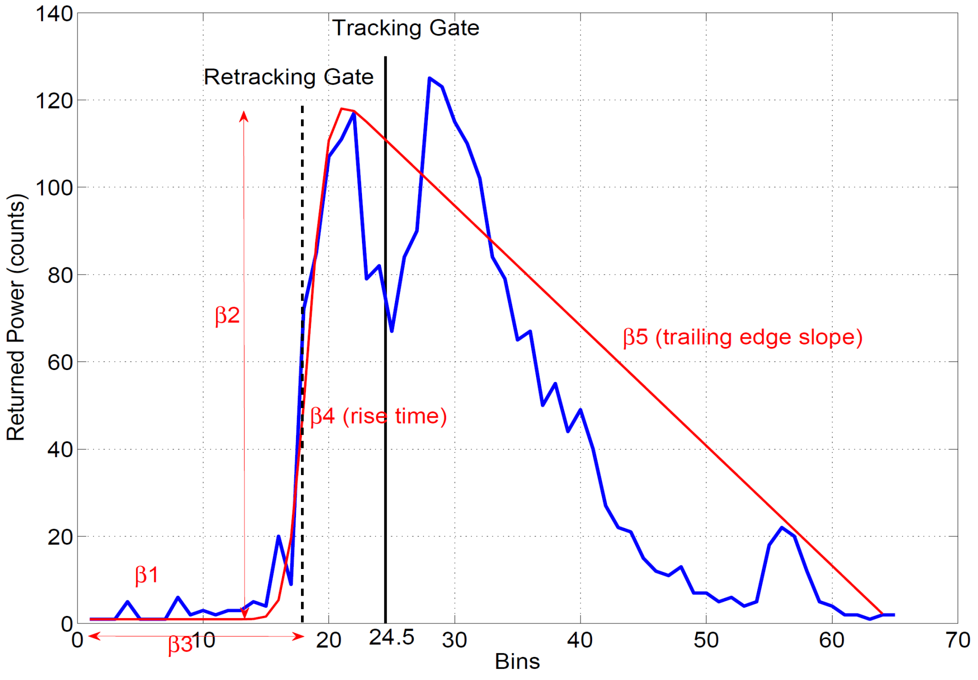

Figure 3.7: *5β-parameter retracker fits a single-ramp waveform (Tourian 2013)*

The β-parameter is fitted on the waveform using least squares method to estimate 5 parameters $\beta_1 - \beta_5$. The offset can be derived from the β_3 and the tracking gate, so the range correction can be determined as the following equation:

$$\triangle R_{\mathrm{ret}} = (\beta_3 - \mathrm{Gate}_{\mathrm{nom}}) \cdot \tau \cdot \frac{\mathrm{c}}{2} \tag{3.5}$$

3.4.2 Off Center of Gravity (OCOG) retracker

OCOG is a robust retracker, which depends on the statistical approach. It was introduced by Wingham et al. (1986) to produce ice sheet data products from ERS-1/2. This algorithm calculates center of gravity (OCG) of a rectangular box. The twice of OCG height is called waveform amplitude A, and it determines the length of the box. The width (W) of the rectangular box determines the retracking gate, which shown in Figure 3.8.

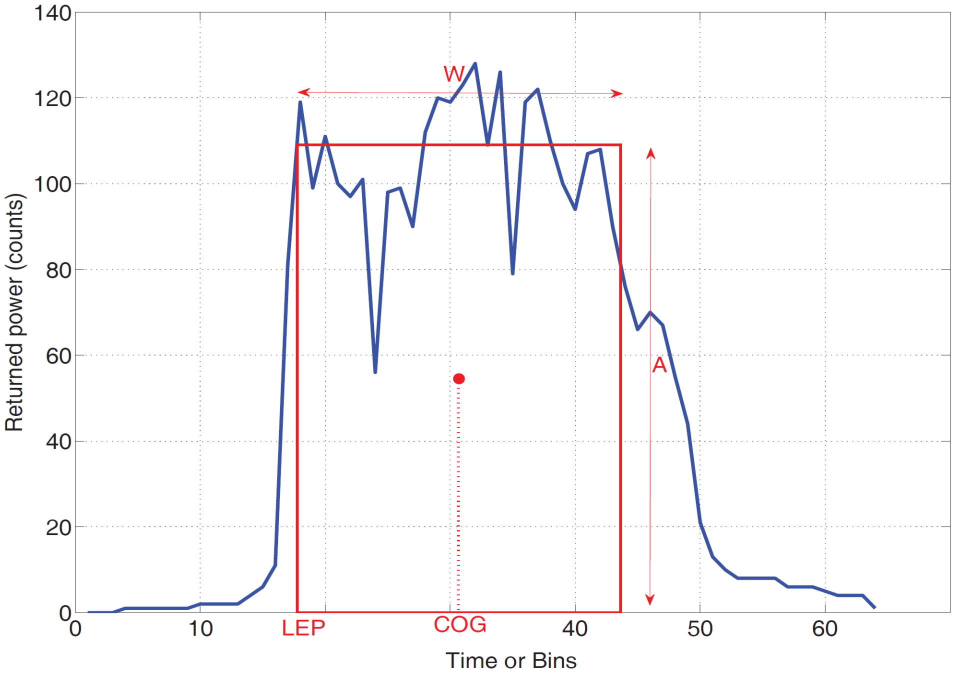

Figure 3.8: Schematic description of OCOG retracker (Tourian 2012)

The function to determine COG, A and W are given by the following equations:

$$\mathrm{COG} = \sum_{\mathrm{i}=1+\mathrm{n}_1}^{\mathrm{N}-\mathrm{n}_2} \mathrm{iP}_\mathrm{i}^2(\mathrm{t}) \Bigg/ \sum_{\mathrm{i}=1+\mathrm{n}_1}^{\mathrm{N}-\mathrm{n}_2} \mathrm{P}_\mathrm{i}^2(\mathrm{t}) \tag{3.6}$$

$$A = \sqrt{\sum_{i=1+n_1}^{N-n_2} P_i^4(t) \Bigg/ \sum_{i=1+n_1}^{N-n_2} P_i^2(t)} \tag{3.7}$$

$$W = \left(\sum_{i=1+n_1}^{N-n_2} P_i^2(t) \right)^2 \Bigg/ \sum_{i=1+n_1}^{N-n_2} P_i^4(t) \tag{3.8}$$

in which, P_i is the waveform power at i bin, N is the total number of samples in the waveform. n_1 and n_2 are the numbers of bins in the waveform affected by aliasing at the beginning and the end. Then, the retracking gate can be calculated by:

$$\mathrm{Gate_{ret}} = \mathrm{COG} - \frac{\mathrm{W}}{2} \quad . \tag{3.9}$$

Chapter 4

Data and area of study

In this thesis, we use Sentinel-3 SRAL data and Landsat-8 satellite images for the aims of the study. These data are available from the websites of their operators, which are free to the public. We selected the first two largest lakes (Dongting Lake and Poyang Lake) in China for the experiments.

4.1 Data

4.1.1 Altimetry data

The Sentinel-3 orbit has a revisit time of 27 days providing global coverage of topography data at mesoscale (inter-track distance at the Equator 104 km using one satellite). The along-track resolution and across-track resolution of SAR mode are approximately 300 m and 1.64 km respectively. Sentinel-3 SRAL data, distributed by ESA, fulfills needs of the most scientific researchers. The data include time of range measurements, on-board tracked ranges, satellite positions, geophysical corrections and instrumental corrections. For the range measurements different retracking algorithms, i.e. ocean, 5-β, OCOG are operationally applied to waveforms to provide accurate height estimates.

4.1.2 Satellite images

Combining the altimetry data with satellite images is very beneficial to monitor the water body surface. As mentioned in Chapter 2, Sentinel-3A also carries many other instruments except altimeter, including Ocean and Land Colour Instrument (OLCI). OLCI images have 21 spectral bands with wavelengths ranging from the optical to the near-infrared. OLCI image is supposed to be used for our study, because the two sensors (SRAL and OLCI) are carried on the same satellite mission, which can provide synchronous altimetry measurments and images. However, the resolution is unsatisfied, which is 300 m. Due to the along-track resolution of altimetry of 20 Hz is approximately 300 m, so the spatial error can be very large. Consequently, it is not significant for monitoring water bodies with that kind of image, as shown in Figure 4.1.

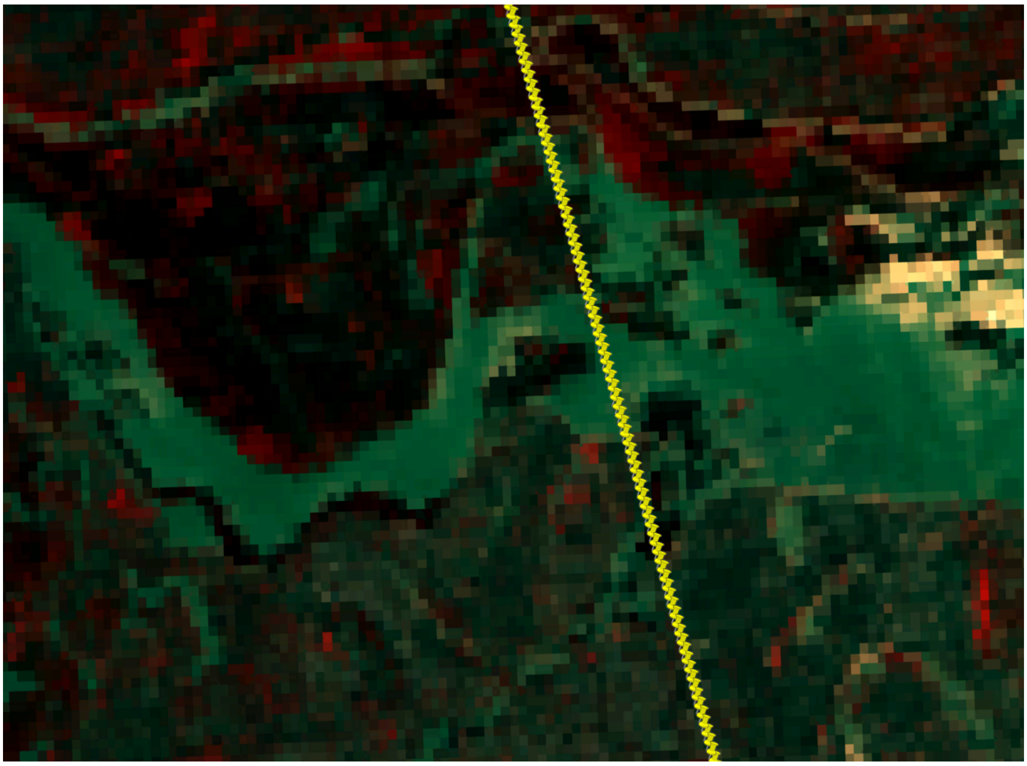

Figure 4.1: *Image and altimetry measurements from Sentinel-3A on 19 July 2018*

Landsat-8 launched on February 11, 2013, is operated by the National Aeronautics and Space Administration (NASA) and the United States Geological Survey (USGS). The Landsat-8 satellite payload consists of two science instruments, which are the Operational Land Imager (OLI) and the Thermal Infrared Sensor (TIRS). These two sensors provide seasonal coverage of the global landmass at a spatial resolution of 30 m (visible, NIR, SWIR), 100 m (thermal), and 15 m (panchromatic). The following table 4.1 shows the spatial resolution of each band. Landsat-8 acquires 550 scenes per day globally, and the revisit period is 16 days.

Table 4.1: *Resoulution of each band of Landsat-8 OLI and TIRS*

(Markham et al. 2013)

Landsat-8 OLI and *TIRS* Bands (μm)		
30 m Coastal/ Aerosol	0.435 - 0.451	Band 1
30 m Blue	0.452 - 0.512	Band 2
30 m Green	0.533 - 0.590	Band 3
30 m Red	0.636 - 0.673	Band 4
30 m NIR	0.851 - 0.879	Band 5
30 m SWIR-1	1.566 - 1.651	Band 6
30 m SWIR-2	2.107 - 2.294	Band 7
15 m Pan	0.503 - 0.676	Band 8
30 m Cirrus	1.363 - 1.384	Band 9
100 m TIR-1	10.60-11.19	Band 10
100 m TIR-2	11.50-12.51	Band 11

For this study, we use Landsat-8 RGB bands of each image. Since the temporal resolution is higher than that of Sentinel-3, the acquisition date of each image should be as close as the date of altimetry data. The spatial resolution is 15 m in panchromatic band, which is higher than the other bands, hence we implement pansharpening to create high-resolution color images in order to increase the quality of images. Pansharpening is a process of merging high-resolution panchromatic (Band 8) and lower resolution multispectral (Band 2, 3 and 4) imagery to create a single high-resolution color image. Figure 4.2(a) and 4.2(b) shows the performance of the RGB image before and after pansharpening.

(a) *The original RGB image*

(b) *The RGB image after pansharpening*

Figure 4.2: *The color image before and after pansharpening*

4.2 Study area

4.2.1 Dongting Lake

Dongting Lake is located in northeastern Hunan province, China. It is a flood basin of the Yangtze River. Hence the lake's size depends on the season. In the summer (from July to September) period, flood water from the Yangtze River flows into the lake, enlarging it greatly. The lake's area, which normally is 2 820 square, may increase to 20 000 km^2 in flood season, when a vast amount of water and sediment from the Yangtze River flow into the lake. Once it was the largest freshwater lake in China, but due to the 19th century much of the lake's shallow areas had been destroyed to create farmland. After 1949 a new round of wetland drainage was destroyed, which left only a fraction of the original wetland intact. Some of those areas have subsequently been returned to wetland conditions. As the water level is variable in different seasons, this lake is very typical for monitoring inland surface water body researches. Figure 4.3 and Figure 4.4 present the location and the Sentinel-3A track of the lake.

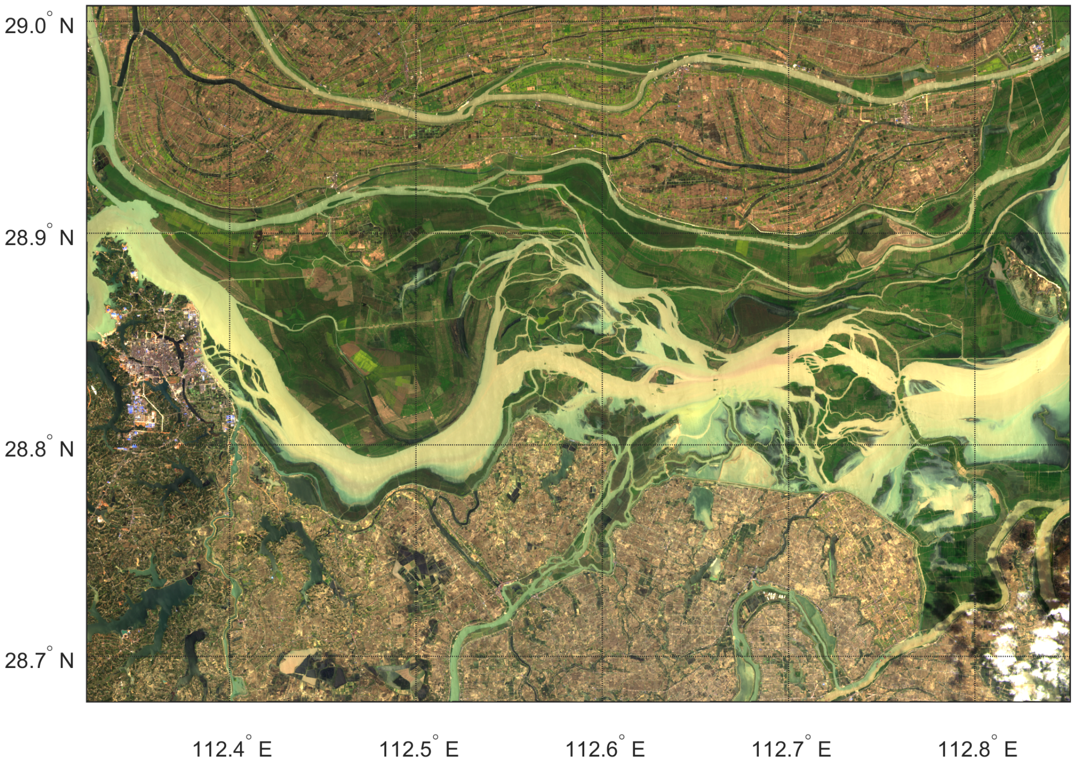

Figure 4.3: *Location of Dongting Lake*

S-3A Pass No. 619

Relative Orbit Number	310
Pass Number	619
Asc/Desc Pass	Ascending
Orbit Start ANX Longitude	119.37 deg

Figure 4.4: Ground track of Sentinel-3A across Dongting Lake (HydroSat Website)

4.2.2 Poyang Lake

Poyang Lake located in Jiangxi Province, is the largest freshwater lake in China. The lake is fed by the Gan, Xin, and Xiu rivers, and it connects to the Yangtze through a channel. The area of Poyang Lake fluctuates dramatically between the wet and dry seasons, but in recent years the size of the lake has been decreasing overall. In a normal year the area of the lake averages 3 500 km^2. In early 2012, due to drought, sand quarrying, and storing water at the Three Gorges Dam, the area of the lake reached a low of about 200 km^2. Due to the Three Gorges Dam upriver on the Yangtze river, Poyang Lake can shrink and dry up for portions of the year. Figure 4.5 and Figure 4.6 present the location and the Sentinel-3A track of the lake.

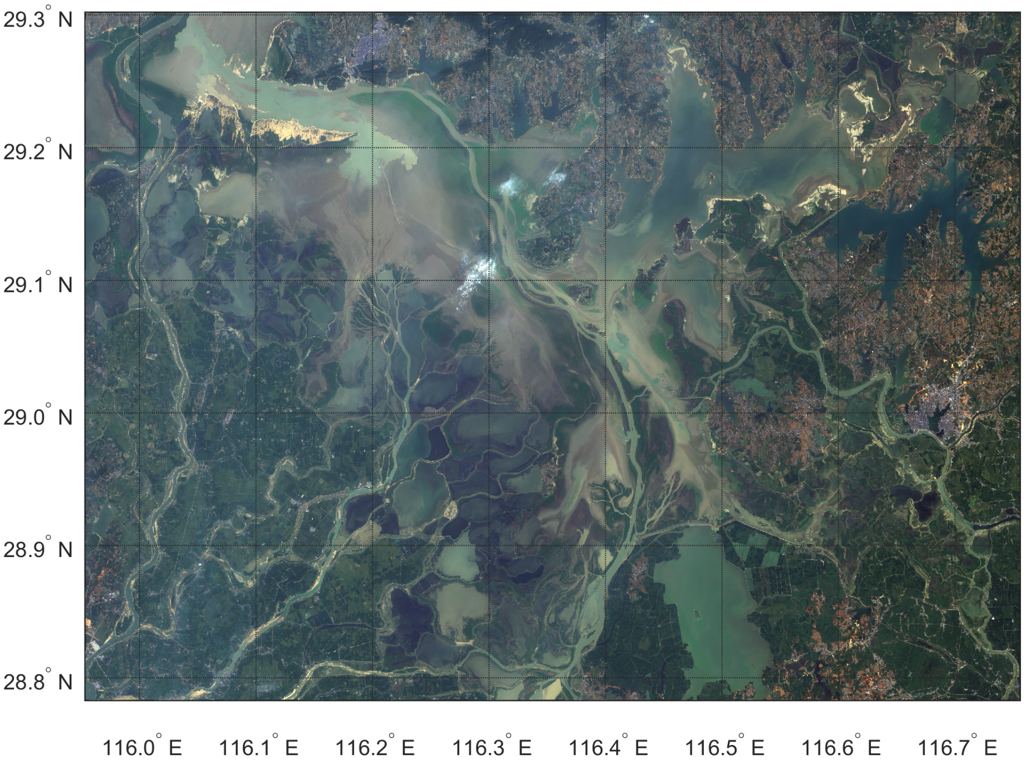

Figure 4.5: *Location of Poyang Lake*

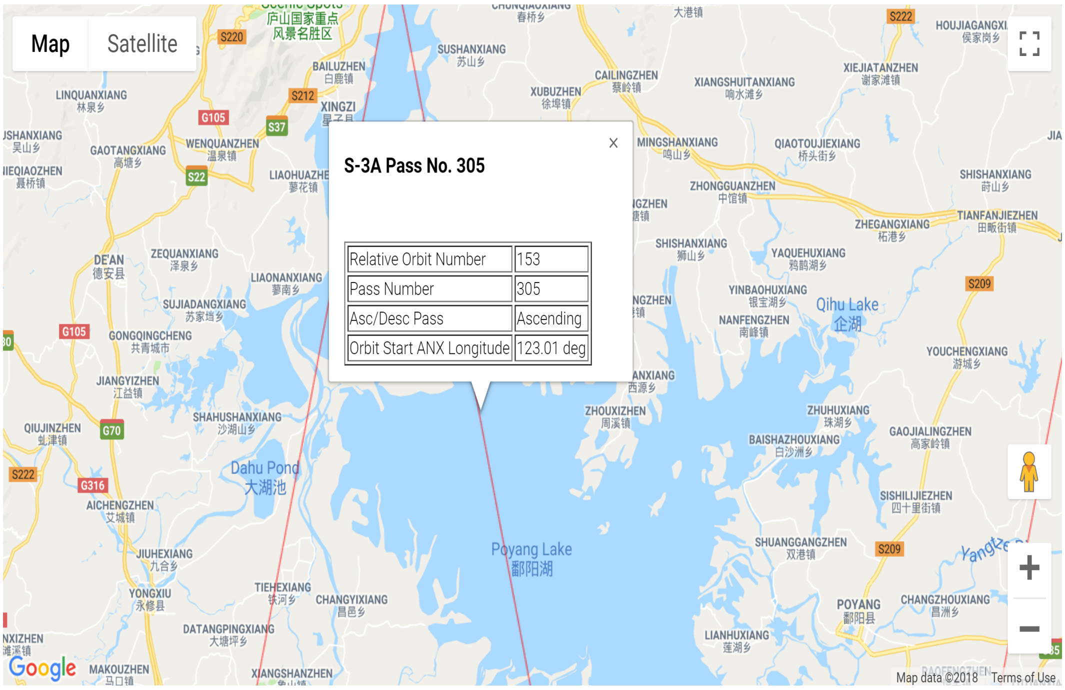

S-3A Pass No. 305

Relative Orbit Number	153
Pass Number	305
Asc/Desc Pass	Ascending
Orbit Start ANX Longitude	123.01 deg

Figure 4.6: *Ground track of Sentinel-3A across Poyang Lake (HydroSat Website)*

Chapter 5

Methodology

5.1 Virtual station creation

A virtual station is defined when a satellite ground track intersects with water bodies. The position of a virtual station is the intersection point between the centre of the search circle and satellite ground track. A search radius depends on the size of a water body for data retrieve. Each time the satellite passes over the water body, the tracks of different sampling dates will not be at the same position, and the water width is also different in different seasons (Figure 5.1). Therefore, the position of virtual station will be different on each sampling date. In order to get more accurate range measurements and avoid hooking effect, water and land surfaces are suggested to be clearly distinguished. With the help of aforementioned satellite images obtained from Landsat-8, it can determine the accurate position and the search radius of the virtual station of each sampling date.

Figure 5.2 shows the chosen principle of a virtual station and search radius. The water level time series at the virtual station locations are then obtained by averaging the measurements inside the search circles. This process guarantees that we select the waveforms of these measurements with a sharp leading edge, for which the performance of retracking algorithms are the best.

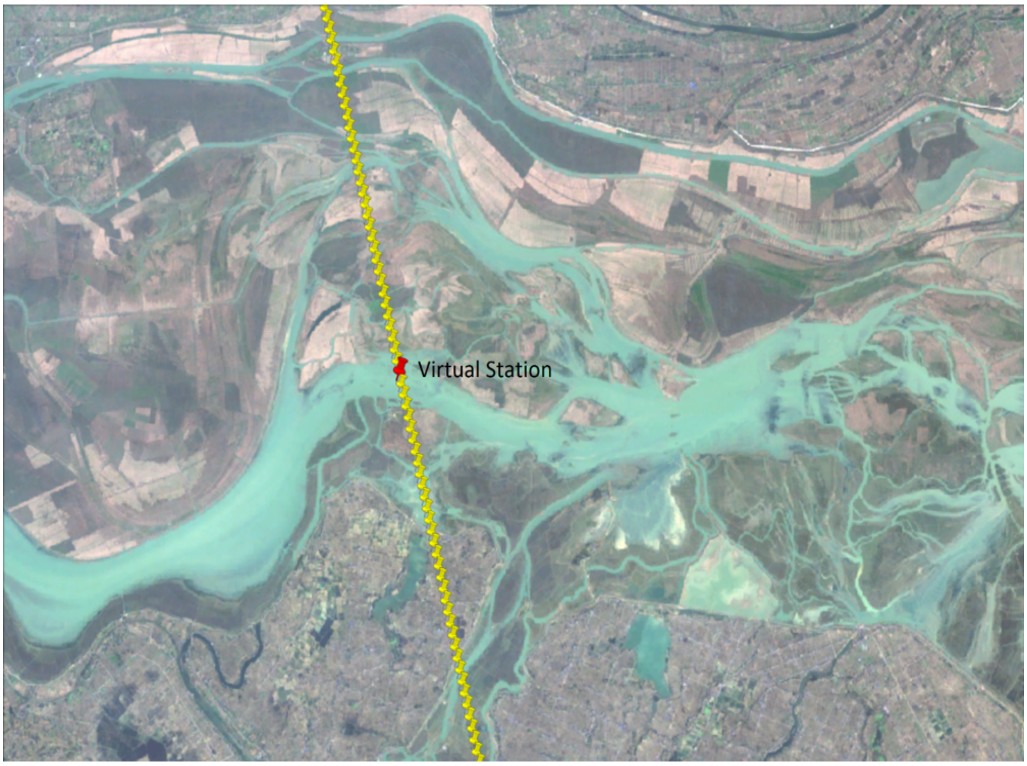

(a) *22 January 2017*

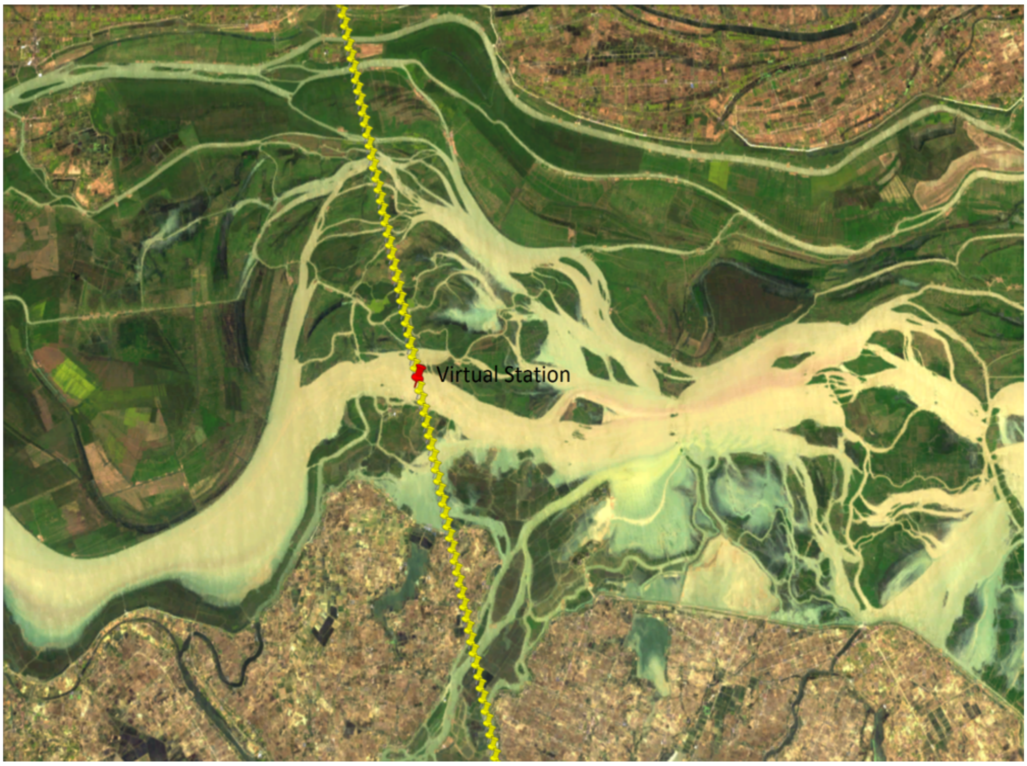

(b) *27 March 2017*

Figure 5.1: *The ground track over Dongting Lake in different seasons*

(c) *18 August 2017*

Figure 5.1: *The ground track over Dongting Lake in different seasons*

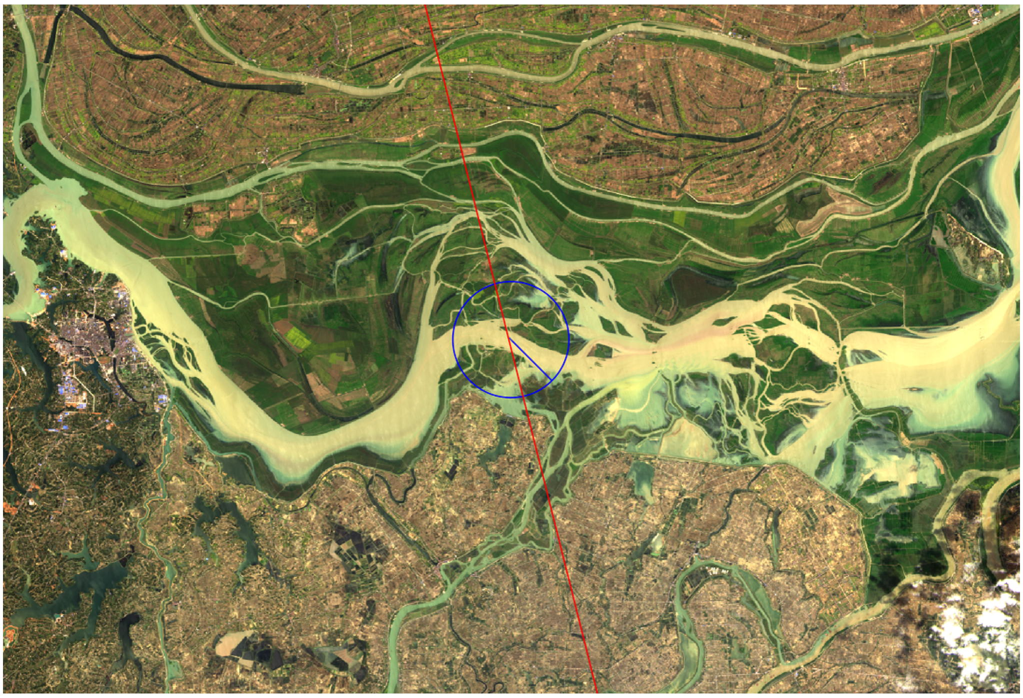

Figure 5.2: *Schematic of selection principle of virtual station and search radius*

5.2 Water level generation

After determination of measurements inside virtual station circles, the next step we should retrack the waveforms of these measurements to get accurate range. However, the retracked range ($\hat{R}$) contains some errors as mentioned in Chaper 2. To calculate the water level with respect to the geoid, we should remove these errors, i.e. geophysical adjustments. The water level generation equation (eq. (5.1)) is derived from the altimetry data according to eq. (2.3):

$$\begin{aligned} h =& H_{\text{sat}} - \hat{R} + \sum_i \Delta R_i \\ =& H_{\text{sat}} - \hat{R} + \Delta C_{\text{dtc}} + \Delta C_{\text{wtc}} + \Delta C_{\text{ion}} + \Delta C_{\text{ib}} + \\ & \Delta C_{\text{ssb}} + \Delta C_{\text{pt}} + \Delta C_{\text{ot}} + \Delta C_{\text{et}} + \text{GH} \ , \end{aligned} \tag{5.1}$$

in which:

ΔC_{dtc}: Dry Tropospheric Correction
ΔC_{wtc}: Wet Tropospheric Correction
ΔC_{ion}: Ionospheric Correction
ΔC_{ib}: Inverse Barometer Correction
ΔC_{ssb}: Sea Sate Bias Correction
ΔC_{pt}: Pole Tide Correction
ΔC_{ot}: Ocean Tide Correction
ΔC_{et}: Earth Tide Correction
GH: Geoid Height

5.3 Outlier rejection

The spatial resolution along the track for 20 Hz altimeter measurements is approximately 300 m, consequently, there are more than 10 measurements inside the virtual station circle of each sampling date. In the idealized condition, the calculated water level from each single measurement should be same in such a small area. However, in reality, outliers may occur sometimes. To improve the accuracy, we use median value ($\tilde{h}$) comparing to each single calculated water level (h), which is the difference (r), as the eq. (5.2):

$$r = h - \tilde{h} \ . \tag{5.2}$$

Initially, the tolerance of the difference should be defined, if the absolute value of r is larger than the tolerance, hence the measurement can be regarded as the outlier, which should be rejected. After several iterations, the remaining measurements without outliers derive the water level with the mean value ($\bar{h}$).

5.4 Performance metrics

In order to quantify the dispersion of a set of data values, we referred the standard deviation (σ). For each sampling date, there is a set of data which has rejected outliers as mentioned above. To evaluate the bias within the set of data A, the standard deviation is calculated as eq. (5.3):

$$\sigma = \sqrt{\frac{\sum_{i=1}^{n}(A_i - \bar{A})^2}{n-1}} \,. \tag{5.3}$$

For cross-validation, we compare the time series between our result and the other database. Correlation coefficient gives the description of coincide information between two databases. For dataset A and dataset B, the correlation coefficient (Corr) is shown as follows:

$$\mathrm{Corr} = \frac{\sum_{i=1}^{n}(A_i - \bar{A})(B_i - \bar{B})}{\sqrt{\sum_{i=1}^{n}(A_i - \bar{A})^2 \sum_{i=1}^{n}(B_i - \bar{B})^2}} \,. \tag{5.4}$$

In addition, in this thesis, we have compared the results from different retracking algorithms. The performance can be indicated as Root Mean Square (RMS), concerning the bias between the result (A) and the reference dataset (B), which is evaluated as follow:

$$\mathrm{RMS} = \sqrt{\frac{\sum_{i=1}^{n}(A_i - B_i)^2}{n}} \,. \tag{5.5}$$

Chapter 6

Experiments and validations

In this chapter, we have generated the water level time series over Dongting Lake and Poyang Lake. Initially, among all the on-board retrackers of Sentinel-3A altimetry mission, we use Ocean retracked ranges to calculate the water level and standard deviation of each date. The standard deviation of each implementation is also given in the time series and a seperate scatter plot. However, due to the lack of the data from the gauge stations, we use water level time series provided by DAHITI for comparison. The Database for Hydrological Time Series of Inland Waters (DAHITI) was developed by Technical University of Munich, which provides water level time series of lakes, reservoirs, rivers, and wetlands derived from multi-mission satellite altimetry for hydrological applications. As the DAHITI database derived from several different altimetry missions, the temporal resolution is different from that of Sentinel-3A, hence the comparison seems to be arduous. In order to get the correlation of the water level time series between two databases (Sentinel-3A and DAHITI), we use the method of interpolation. Accordingly, the data from DAHITI can be interpolated to the same sampling dates as Sentinel-3A.

We also retrack the waveforms with 5β and OCOG retracking algorithms to generate water level time series. Then compare the results from different estimation algorithms with, and check the shape of waveforms to see if the algorithms are capable to a specified type of waveforms.

6.1 Dongting Lake

For Dongting Lake, we use 31 repeated cycles to generate the water level time series from June 23, 2016 to September 11, 2018. The red bar of each time epoch shows the standard deviation of the measurements. Here, we can see the water level varies seasonally. The highest level appears in July for three years, more than 30 meters, and the lowest level appears in December or January. As the description of Dongting Lake in Chapter 4, it coincides with the plotted water level variation.

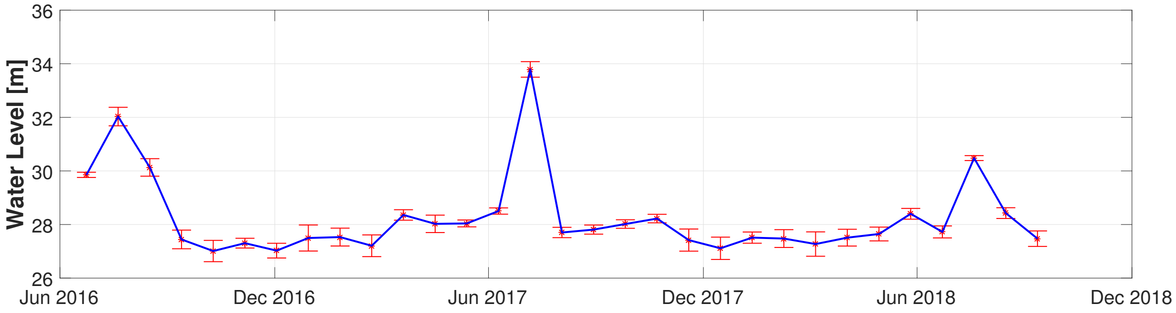

Figure 6.1: *Time series with standard deviation of Dongting Lake*

From Figure 6.1, we can see the range of the standard deviation is mainly located between 10 and 30 cm. The maximum, minimum and average value of standard deviation are 49 cm, 9 cm and 27 cm respectively. Afterwards, within the same period of time, water level time series from Sentinel-3A and DAHITI database are plotted in a joint way (Figure 6.2).

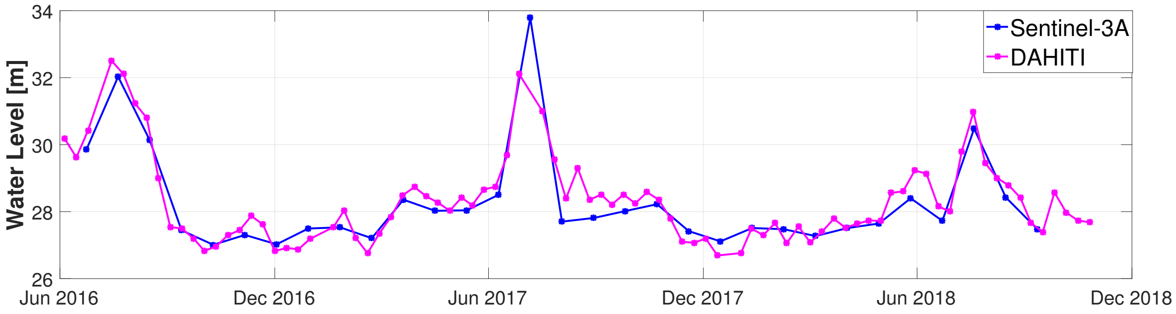

Figure 6.2: *Time series comparison between Sentinel-3A and DAHITI of Dongting Lake*

The seasonal and annual variations are quite coincident between Sentinel-3A and DAHITI, and the correlation coefficient is 0.93. However, the highest water level of Sentinel-3A and DAHITI in July 2017 are 33.79 m and 32.11 m respectively. The water level difference between the two databases in July 2017 is very large, which is more than 1.5 m. We cannot recognize that if the flood crest came on that sampling date of Sentinel-3A or the retracking algorithm is not suitable to the waveforms. In order to explore the discrepancy, we used 5β and OCOG retracking algorithms to retrack the waveforms respectively, and the results are plotted in Figure 6.3.

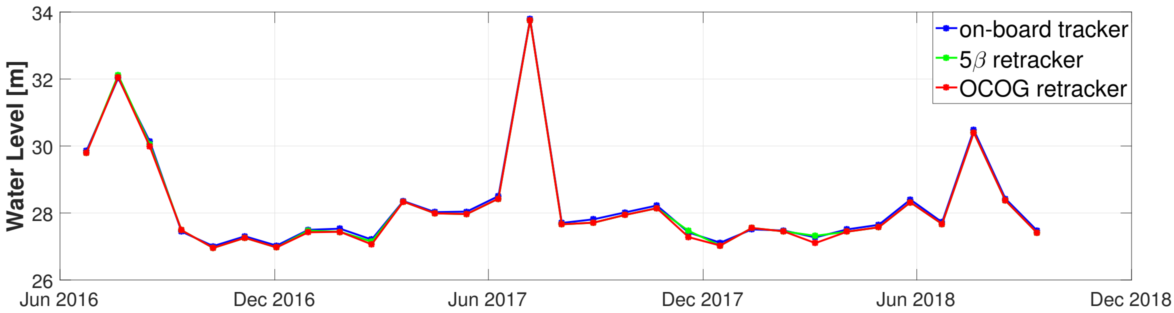

Figure 6.3: *Time series comparison with different retracking algorithms of Dongting Lake*

We can see that different retrackers give almost same results comparing to the on-board Ocean tracker. The parameters of the comparison with on-board retracker are shown in the table 6.1.

Table 6.1: *Retracked results compared with on-board retracker*

Retracker	Correlation	RMS [cm]
5β	0.99	6.3
OCOG	0.99	8.0

Here, we selected two sampling dates randomly to check the type of waveforms, one is in the winter season, and the other one is in the summer season. In the following figures (Figure 6.4 and 6.5), we plotted the shape of waveforms in the lake area, and the waveforms are normalized. The positions of measurements (Figure 6.4(a) and 6.5(a)) in blue color are the data we used to generate the water level in the virtual station search circle, and figures (6.4(b) and 6.5(b)) in blue color are the corresponding waveforms in the virtual station search circle. As we expected, the waveforms corresponding to the measurements over the land surface are contaminated, and over the water surfaces the waveforms are regular and clear. It is obvious that most waveforms in this area belong to the Quasi-Specular model, i.e. the waveform has only one sharp peak. All these three retracking algorithms seem to be applicable for this kind of waveform.

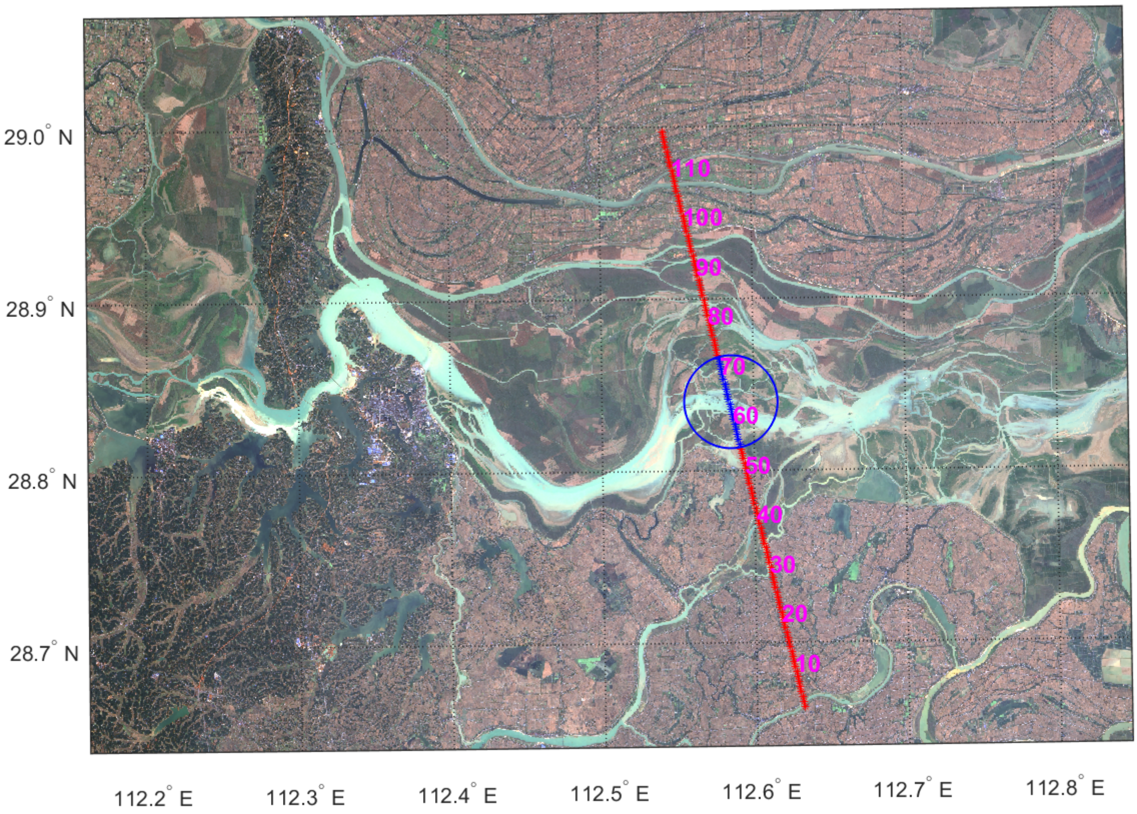

(a) *RGB image of 5 December 2016*

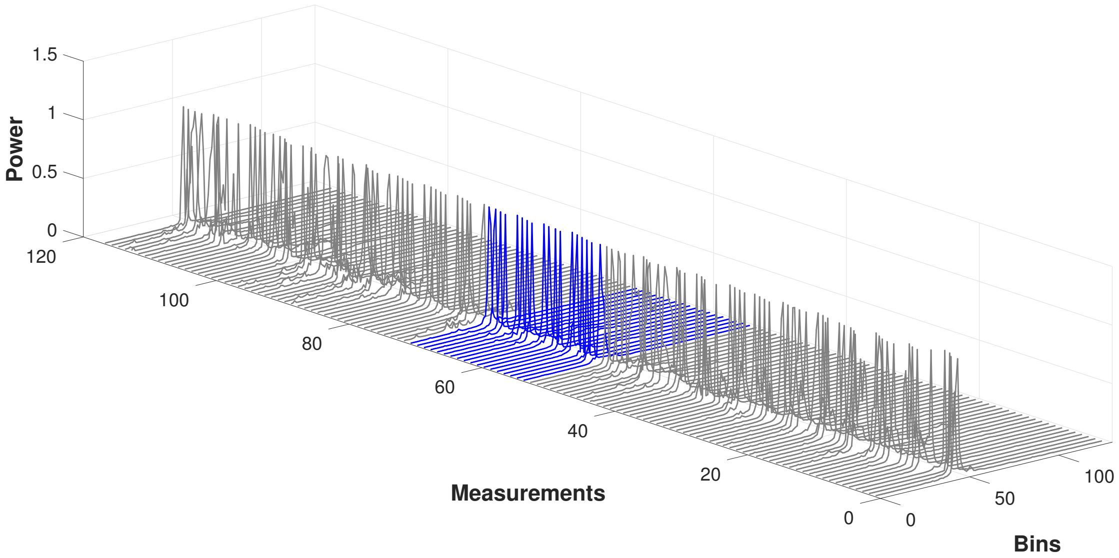

(b) *Waveforms of 2 December 2016*

Figure 6.4: *The waveforms combined with the image in winter season*

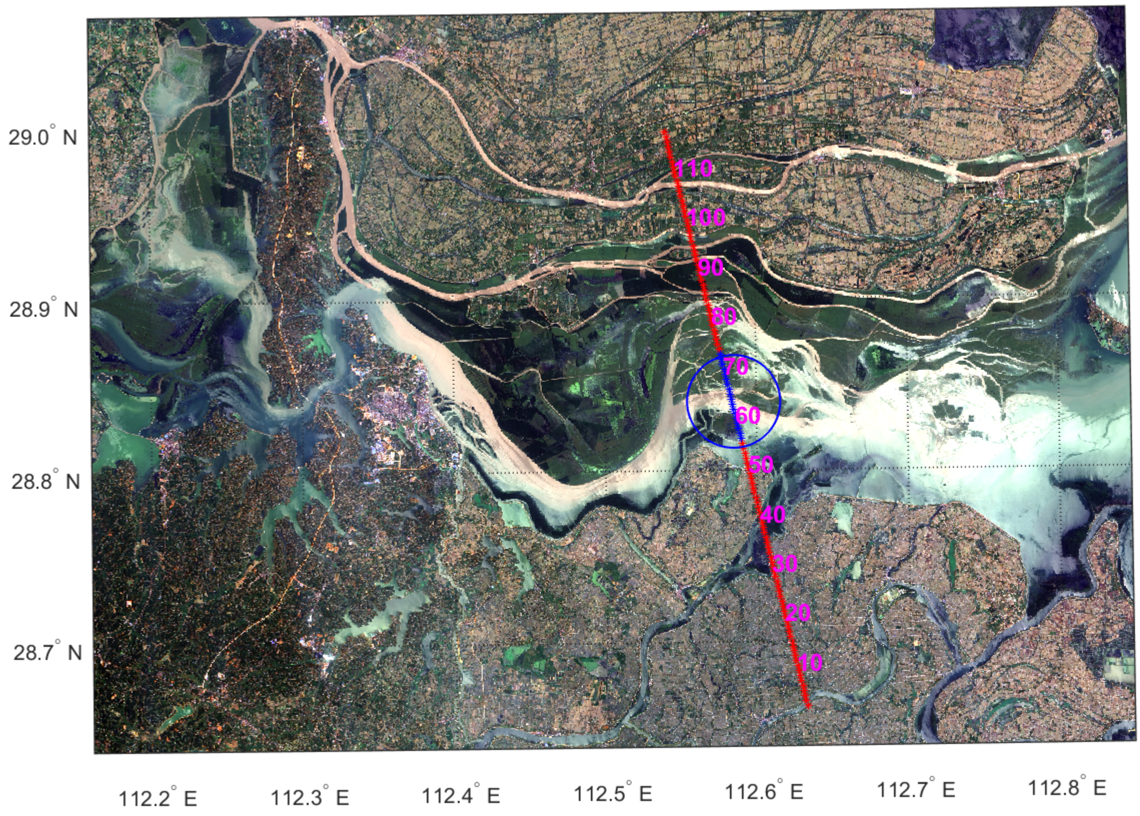

(a) *RGB image of 20 July 2018*

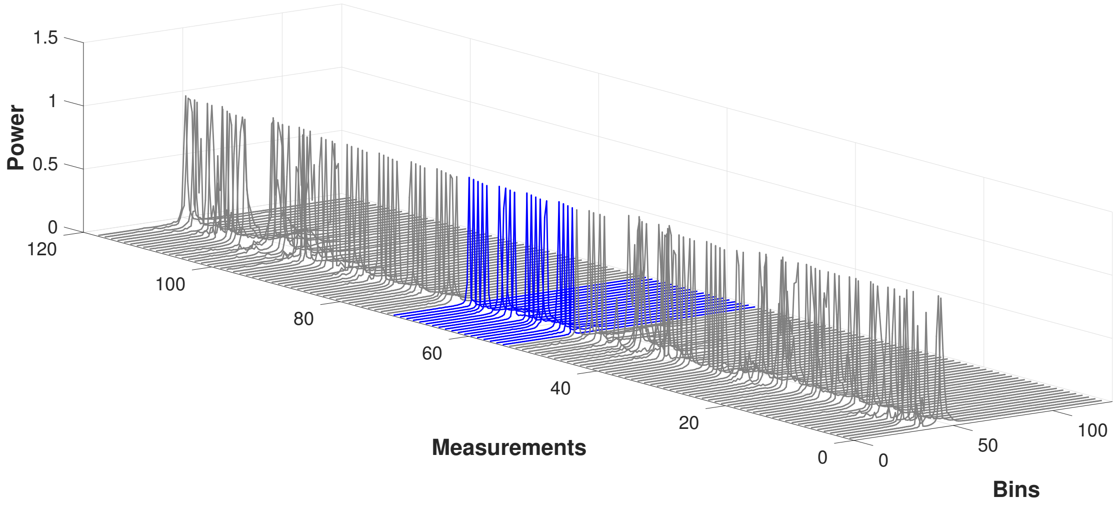

(b) *Waveforms of 19 July 2018*

Figure 6.5: *The waveforms combined with the image in summer season*

6.2 Poyang Lake

For Poyang Lake, we use 32 repeated cycles to generate the water level time series from July 9, 2016 to October 24, 2018. Same as Dongting Lake, the water level time series with standard deviation of each date are shown in Figure 6.6. Similarly, the highest level appears in July or August in each year.

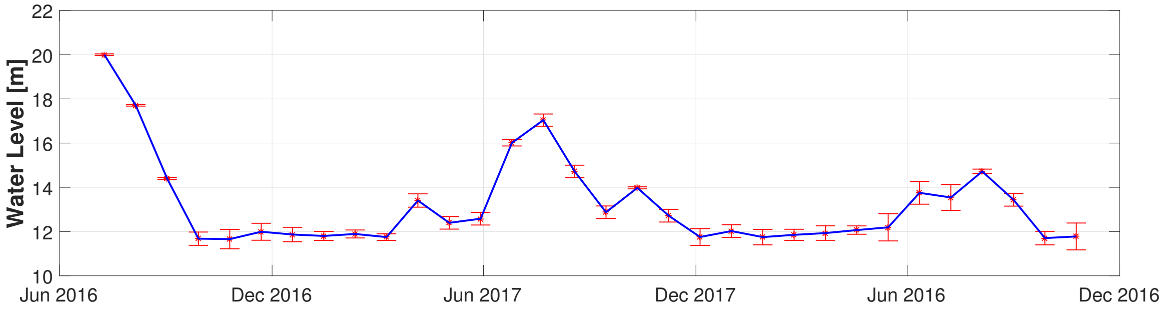

Figure 6.6: *Time series with standard deviation of Poyang Lake*

We can see the range of standard deviation mainly below 20 cm, and the maximum standard deviation is 44 cm. Due to DAHITI has no data for Poyang Lake after July 8, 2017, hence we just compare the time series from July 2016 to July 2018. The water level time series from two datasets are shown in Figure 6.7.

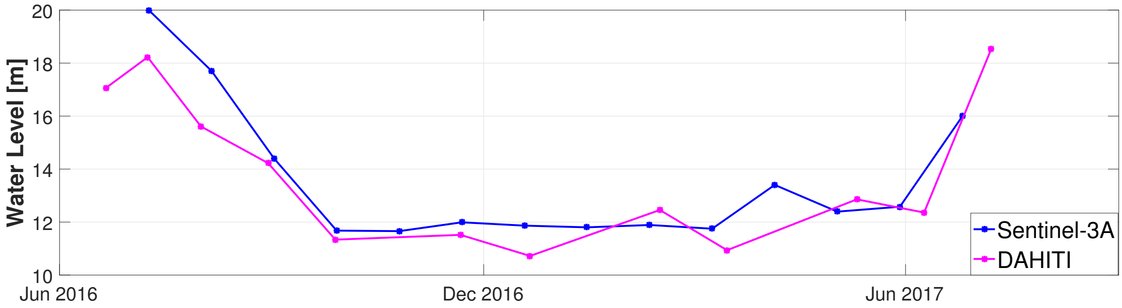

Figure 6.7: *Time series comparison between Sentinel-3 and DAHITI of Poyang Lake*

Although the the seasonal trend is similar to the result of Sentinel-3A, the height discrepancy is quite large on some sampling dates. From the statistics, the correlation coefficient is 0.95. There are 3 same sampling dates with that of DAHITI, i.e. July 9, September 28 and November 21 in 2016. The water level difference on July 9, 2016 is 1.77 m, but on the other two dates the differences are 34 cm and 47 cm. Due to we regarded the DAHITI database as the reference, the difference of 1.77m is extremely large. In order to validate the performance of different retracking algorithms, we also used 5β and OCOG retrackers to implement the waveforms, as the following figure shows.

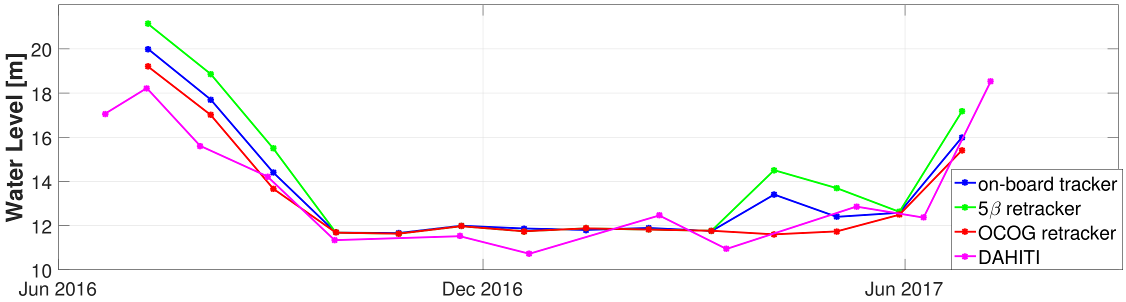

Figure 6.8: *Time series comparison with different retracking algorithms of Poyang Lake*

The two different retrackers give quite different results. From Figure 6.8, we can see the differences of water level on July 9, 2016 and April 5, 2017 are very large. However, on September 28 and November 21 in 2016, the differences are almost same. Moreover, the result of OCOG retracker on July 9, 2016 is much closer to the corresponding value of DAHITI. The water level difference between OCOG algorithm and DAHITI is 79 cm on July 9, 2016, which is a large improvement comparing to the other two algorithms. The parameters of the comparison with on-board Ocean tracker are shown in the table 6.2.

Table 6.2: *Retracked results compared with on-board retracker*

Retracker	Correlation	RMS [cm]
5β	0.99	76.2
OCOG	0.98	64.0

Here, we select these sampling dates with large and small water level differences, to check the type of waveforms, which is shown in the following figures (Figure 6.9 and 6.10).

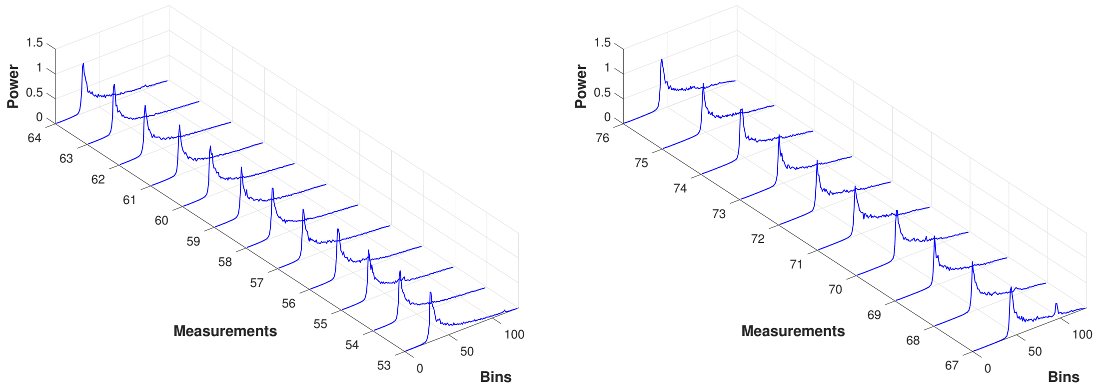

(a) *Waveforms of 9 July 2016*

(b) *Waveforms of 5 April 2017*

Figure 6.9: *Waveforms of two dates with large difference among three algorithms*

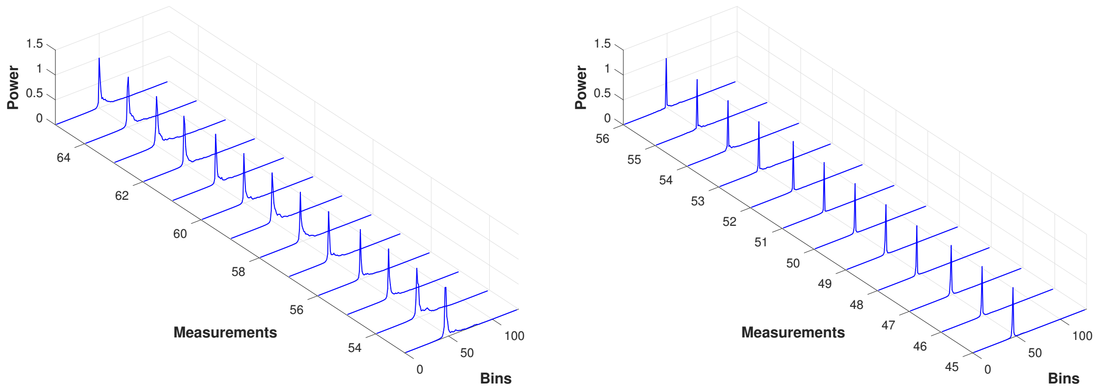

(a) *Waveforms of 28 September 2016*

(b) *Waveforms of 21 November 2016*

Figure 6.10: *Waveforms of two dates with small difference among three algorithms*

The waveforms obtained on July 9, 2016 and April 5, 2017 belong to flat patch model (Figure 6.9). However, the waveforms obtained on September 28, 2016 and November 21, 2016 belong to Quasi-Specular model (Figure 6.10). This illustrates the fact that, the type of waveforms from a water body can be different in different seasons. As we mentioned in the above section, the performance of three retrackers shows almost same result (Figure 6.8) with Quasi-Specular model, and OCOG retracking algorithm gives the best performance to flat patch model.

Chapter 7

Conclusion and outlook

7.1 Summary and conclusion

As lack of ground gauge stations, the altimetry satellite missions provide a proper choice to monitor the inland water bodies. The application of satellite altimeter over inland surface water bodies has been explored and proven by many researches. From previous researches, retracking algorithms are implemented to improve the quality of water level time series over inland water bodies. In this thesis, we studied two large lakes in China using altimeter measurements combined with satellite images to determine the best measurements inside the virtual station. We also used different retracking algorithms to compare the results with other database, and check the waveforms of each sampling date.

From the experiments of the two cases, we have investigated the following conclusions:

- With the help of satellite images, we can get accurate positions of virtual stations and the proper measurements inside the search circle.
- A water body may presents different types of waveform in different seasons, hence we need to retrack the waveforms with different algorithms.
- An appropriate retracking algorithm for a specified type of waveform can increase the accuracy of water level.
- All the three tracking methods are capable to Quasi-Specular waveforms, and OCOG shows the best result to flat patch waveforms.

7.2 Outlook

Altimetry data have been shown to be applicable to monitor the inland surface water level, but for a single satellite mission, it cannot provide full coverage of the earth's surface, especially small water bodies. In addition, the temporal coverage from Sentinel-3 is 27 days, there is a high probability that events (e.g. peaks of flood and short term high/low water level variation) cannot be recorded. To overcome this issue, multi-mission could help to improve the monitoring temporal and spatial resolutions.

To classify the waveforms into different types, it is feasible to lead methods of pattern recognition into the classification, and retrack the particular waveform with the proper retracking algorithm.

In order to obtain a superior optical satellite imagery, atmospheric correction should be added to the georeferenced image to remove cloud coverage, but the process procedure should use images from different acquisition dates, which probably cause difference of the real water surface on that day. Further work should look at the possibility of SAR image because of no affections of the cloud.

References

Berry, P., Garlick, J., Freeman, J. & Mathers, E. (2005), 'Global inland water monitoring from multi-mission altimetry', *Geophysical Research Letters* **32**(16).
URL: *https://doi.org/10.1029/2005GL022814*

Bevis, M., Businger, S., Herring, T. A., Rocken, C., Anthes, R. A. & Ware, R. H. (1992), 'Gps meteorology: Remote sensing of atmospheric water vapor using the global positioning system', *Journal of Geophysical Research: Atmospheres* **97**(D14), 15787–15801.
URL: *https://doi.org/10.1029/92JD01517*

Birkett, C. (1994), 'Radar altimetry: a new concept in monitoring lake level changes', *Eos, Transactions American Geophysical Union* **75**(24), 273–275.
URL: *https://doi.org/10.1029/94EO00944*

Birkett, C. (1995), The global remote sensing of lakes, wetlands and rivers for hydrological and climate research, *in* 'Geoscience and Remote Sensing Symposium, 1995. IGARSS'95.'Quantitative Remote Sensing for Science and Applications', International', Vol. 3, IEEE, pp. 1979–1981.
URL: *https://doi.org/10.1109/IGARSS.1995.524084*

Boergens, E., Dettmering, D., Schwatke, C. & Seitz, F. (2016), 'Treating the hooking effect in satellite altimetry data: A case study along the mekong river and its tributaries', *Remote Sensing* **8**(2), 91.
URL: *https://doi.org/10.3390/rs8020091*

Brown, G. (1977), 'The average impulse response of a rough surface and its applications', *IEEE transactions on antennas and propagation* **25**(1), 67–74.
URL: *http://doi.org/10.1109/TAP.1977.1141536*

Calmant, S. & Seyler, F. (2006), 'Continental surface waters from satellite altimetry', *Comptes Rendus Geoscience* **338**(14-15), 1113–1122.
URL: *https://doi.org/10.1016/j.crte.2006.05.012*

Cazenave, A., Bonnefond, P., Dominh, K. & Schaeffer, P. (1997), 'Caspian sea level

from topex-poseidon altimetry: Level now falling', *Geophysical Research Letters* **24**(8), 881–884.
URL: *https://doi.org/10.1029/97GL00809*

Chelton, D., Ries, J., Haines, B., Lee, F. & Callahan, P. (2001), 'Satellite altimetry. chapter 1, in" satellite altimetry and earth sciences"'.
URL: *https://doi.org/10.1016/S0074-6142(01)80146-7*

Cooley, H. (2006), *Floods and droughts*, Island Press: Washington, DC, USA.

Crétaux, J.-F. & Birkett, C. (2006), 'Lake studies from satellite radar altimetry', *Comptes Rendus Geoscience* **338**(14-15), 1098–1112.
URL: *https://doi.org/10.1016/j.crte.2006.08.002*

Crétaux, J.-F., Jelinski, W., Calmant, S., Kouraev, A., Vuglinski, V., Bergé-Nguyen, M., Gennero, M.-C., Nino, F., Del Rio, R. A., Cazenave, A. et al. (2011), 'Sols: A lake database to monitor in the near real time water level and storage variations from remote sensing data', *Advances in space research* **47**(9), 1497–1507.
URL: *https://doi.org/10.1016/j.asr.2011.01.004*

Da Silva, J. S., Calmant, S., Seyler, F., Rotunno Filho, O. C., Cochonneau, G. & Mansur, W. J. (2010), 'Water levels in the amazon basin derived from the ers 2 and envisat radar altimetry missions', *Remote sensing of environment* **114**(10), 2160–2181.
URL: *https://doi.org/10.1016/j.rse.2010.04.020*

Davis, J., Herring, T., Shapiro, I., Rogers, A. & Elgered, G. (1985), 'Geodesy by radio interferometry: Effects of atmospheric modeling errors on estimates of baseline length', *Radio science* **20**(6), 1593–1607.
URL: *https://doi.org/10.1029/RS020i006p01593*

Deng, X. (2003), *Improvement of geodetic parameter estimation in coastal regions from satellite radar altimetry*, Curtin University of Technology.

Dumont, J., Rosmorduc, V., Picot, N., Desai, S., Bonekamp, H., Figa, J., Lillibridge, J. & Scharroo, R. (2009), 'Ostm/jason-2 products handbook', *NOAA/NESDIS: Polar Series/OSTM J* **400**(1).

Eakins, B. & Sharman, G. (2010), 'Volumes of the world's oceans from etopo1', *NOAA National Geophysical Data Center, Boulder, CO* **7**.

Elmi, O., Tourian, M. J. & Sneeuw, N. (2015), River discharge estimation using

channel width from satellite imagery, *in* '2015 IEEE International Geoscience and Remote Sensing Symposium (IGARSS)', IEEE, pp. 727–730.
URL: *https://doi.org/10.1109/IGARSS.2015.7325867*

Fekete, B. M. & Vörösmarty, C. J. (2007), 'The current status of global river discharge monitoring and potential new technologies complementing traditional discharge measurements', *IAHS publ* **309**, 129–136.

Fernandes, M. J., Lázaro, C., Nunes, A. L. & Scharroo, R. (2014), 'Atmospheric corrections for altimetry studies over inland water', *Remote Sensing* **6**(6), 4952–4997.
URL: *https://doi.org/10.3390/rs6064952*

Fu, L.-L. & Cazenave, A. (2000), *Satellite altimetry and earth sciences: a handbook of techniques and applications*, Vol. 69, Elsevier.

Ghosh, S., Thakur, P. K., Sharma, R., Nandy, S., Garg, V., Amarnath, G. & Bhattacharyya, S. (2017), 'The potential applications of satellite altimetry with saral/altika for indian inland waters', *Proceedings of the National Academy of Sciences, India Section A: Physical Sciences* **87**(4), 661–677.
URL: *https://dx.doi.org/10.1007/s40010-017-0463-5*

Gleick, P. H. (1993), 'Water in crisis', *Pacific Institute for Studies in Dev., Environment & Security. Stockholm Env. Institute, Oxford Univ. Press. 473p* **9**.
URL: *https://www.popline.org/node/340598*

Guo, J., Chang, X., Gao, Y., Sun, J. & Hwang, C. (2009), 'Lake level variations monitored with satellite altimetry waveform retracking', *IEEE journal of selected topics in applied earth observations and remote sensing* **2**(2), 80–86.
URL: *https://doi.org/10.1109/JSTARS.2009.2021673*

Guzkowska, M., Rapley, C., Ridley, J., Cudlip, W., Birkett, C. & Scott, R. (1990), 'Developments in inland water and land altimetry', *ESA contract report 78391881FIFL* .

Iijima, B., Harris, I., Ho, C., Lindqwister, U., Mannucci, A., Pi, X., Reyes, M., Sparks, L. & Wilson, B. (1999), 'Automated daily process for global ionospheric total electron content maps and satellite ocean altimeter ionospheric calibration based on global positioning system data', *Journal of Atmospheric and Solar-Terrestrial Physics* **61**(16), 1205–1218.
URL: *https://doi.org/10.1016/S1364-6826(99)00067-X*

Kang, Z., Tapley, B., Bettadpur, S., Ries, J., Nagel, P. & Pastor, R. (2006), 'Precise

orbit determination for the grace mission using only gps data', *Journal of Geodesy* **80**(6), 322–331.
URL: *https://doi.org/10.1007/s00190-006-0073-5*

Kenny, J. F., Barber, N. L., Hutson, S. S., Linsey, K. S., Lovelace, J. K. & Maupin, M. A. (2009), Estimated use of water in the united states in 2005, Technical report, US Geological Survey.
URL: *https://doi.org/10.3133/cir1344*

Kim, Y., Schmid, T., Charbiwala, Z. M., Friedman, J. & Srivastava, M. B. (2008), Nawms: nonintrusive autonomous water monitoring system, *in* 'Proceedings of the 6th ACM conference on Embedded network sensor systems', ACM, pp. 309–322.
URL: *https://doi.org/10.1145/1460412.1460443*

Kouba, J. (2008), 'Implementation and testing of the gridded vienna mapping function 1 (vmf1)', *Journal of Geodesy* **82**(4-5), 193–205.
URL: *https://doi.org/10.1007/s00190-007-0170-0*

Lee, H., Shum, C., Emery, W., Calmant, S., Deng, X., Kuo, C.-Y., Roesler, C. & Yi, Y. (2010), 'Validation of jason-2 altimeter data by waveform retracking over california coastal ocean', *Marine Geodesy* **33**(S1), 304–316.
URL: *https://doi.org/10.1080/01490419.2010.488982*

Łyszkowicz, A. & Bernatowicz, A. (2017), 'Current state of art of satellite altimetry', *Annual of Navigation* **24**(1), 31–47.
URL: *https://doi.org/10.1515/aon-2017-0003*

Maheu, C., Cazenave, A. & Mechoso, C. R. (2003), 'Water level fluctuations in the plata basin (south america) from topex/poseidon satellite altimetry', *Geophysical research letters* **30**(3).
URL: *https://doi.org/10.1029/2002GL016033*

Markham, B. L., Storey, J. C. & Irons, J. R. (2013), Landsat data continuity mission, now landsat-8: Six months on-orbit, *in* 'Earth Observing Systems XVIII', Vol. 8866, International Society for Optics and Photonics, p. 88661B.
URL: *https://doi.org/10.1117/12.2025290*

Martin, T. V., Zwally, H. J., Brenner, A. C. & Bindschadler, R. A. (1983), 'Analysis and retracking of continental ice sheet radar altimeter waveforms', *Journal of Geophysical Research: Oceans* **88**(C3), 1608–1616.
URL: *https://doi.org/10.1029/JC088iC03p01608*

Mendes, V., Prates, G., Santos, L. & Langley, R. (2000), An evaluation of the accuracy of models for the determination of the weighted mean temperature of the atmosphere, *in* 'Proceedings of ION', pp. 433–438.
URL: *https://doi.org/10400.1/149*

Miller, M., Buizza, R., Haseler, J., Hortal, M., Janssen, P. & Untch, A. (2010), 'Increased resolution in the ecmwf deterministic and ensemble prediction systems', *ECMWF newsletter* **124**, 10–16.

Milzow, C., Krogh, P. E. & Bauer-Gottwein, P. (2011), 'Combining satellite radar altimetry, sar surface soil moisture and grace total storage changes for hydrological model calibration in a large poorly gauged catchment', *Hydrology and Earth System Sciences* **15**(6), 1729–1743.
URL: *https://doi.org/10.5194/hess-15-1729-2011*

Normandin, C., Frappart, F., Diepkilé, A. T., Marieu, V., Mougin, E., Blarel, F., Lubac, B., Braquet, N. & Ba, A. (2018), 'Evolution of the performances of radar altimetry missions from ers-2 to sentinel-3a over the inner niger delta', *Remote Sensing* **10**(6), 833.
URL: *https://doi.org/10.3390/rs10060833*

Pandey, R. K., Crétaux, J.-F., Bergé-Nguyen, M., Tiwari, V. M., Drolon, V., Papa, F. & Calmant, S. (2014), 'Water level estimation by remote sensing for the 2008 flooding of the kosi river', *International journal of remote sensing* **35**(2), 424–440.
URL: *https://doi.org/10.1080/01431161.2013.870678*

Peterson, T. C., Anderson, D., Cohen, S., Cortez-Vázquez, M., Murnane, R., Parmesan, C., Phillips, D., Pulwarty, R. & Stone, J. (2008), 'Why weather and climate extremes matter', *Weather and Climate Extremes in a Changing Climate. Regions of Focus: North America, Hawaii, Caribbean, and US Pacific Islands* pp. 11–33.

Peterson, T. C., Stott, P. A. & Herring, S. (2012), 'Explaining extreme events of 2011 from a climate perspective', *Bulletin of the American Meteorological Society* **93**(7), 1041–1067.
URL: *https://doi.org/10.1175/BAMS-D-12-00021.1*

Ricker, R., Hendricks, S., Helm, V., Gerdes, R., Skourup, H. & Ouwehand, L. (2012), 'Comparison of sea-ice freeboard distribution from aircraft data and cryosat-2', *Proceedings paper* **20**.

Rush, C. (1986), 'Ionospheric radio propagation models and predictions–a mini-review', *IEEE transactions on antennas and propagation* **34**(9), 1163–1170.
URL: *https://doi.org/10.1109/TAP.1986.1143951*

Scharroo, R., Lillibridge, J., Smith, W. & Schrama, E. (2004), 'Cross-calibration and long-term monitoring of the microwave radiometers of ers, topex, gfo, jason, and envisat', *Marine Geodesy* **27**(1-2), 279–297.
URL: *https://doi.org/10.1080/01490410490465265*

Scharroo, R. & Smith, W. H. (2010), 'A global positioning system–based climatology for the total electron content in the ionosphere', *Journal of Geophysical Research: Space Physics* **115**(A10).
URL: *https://doi.org/10.1029/2009JA014719*

Schreiner, W. S., Markin, R. E. & Born, G. H. (1997), 'Correction of single frequency altimeter measurements for ionosphere delay', *IEEE transactions on geoscience and remote sensing* **35**(2), 271–277.
URL: *https://doi.org/10.1109/36.563266*

Schwatke, C., Dettmering, D., Bosch, W. & Seitz, F. (2015), 'Dahiti–an innovative approach for estimating water level time series over inland waters using multi-mission satellite altimetry', *Hydrology and Earth System Sciences* **19**(10), 4345–4364.
URL: *https://doi.org/10.5194/hess-19-4345-2015*

Shum, C., Parke, M., Schutz, B., Abusali, P., Gutierrez, R., Pekker, T., Tapley, B., Benjamin, J. M., Blaha, J., Jacobs, G. et al. (1998), 'Improvement of topex/poseidon altimeter data for global change studies and coastal applications', *AVISO Altimetry Newsletter* **6**, 102–103.

Siddique-E-Akbor, A., Hossain, F., Lee, H. & Shum, C. (2011), 'Inter-comparison study of water level estimates derived from hydrodynamic–hydrologic model and satellite altimetry for a complex deltaic environment', *Remote Sensing of environment* **115**(6), 1522–1531.
URL: *https://doi.org/10.1016/j.rse.2011.02.011*

Sneeuw, N., Lorenz, C., Devaraju, B., Tourian, M. J., Riegger, J., Kunstmann, H. & Bárdossy, A. (2014), 'Estimating runoff using hydro-geodetic approaches', *Surveys in Geophysics* **35**(6), 1333–1359.
URL: *https://doi.org/10.1007/s10712-014-9300-4*

Tourian, M. J. (2012), Controls on satellite altimetry over inland water surfaces

for hydrological purposes, Master's thesis.
URL: *http://dx.doi.org/10.18419/opus-3879*

Tourian, M. J. (2013), *Application of spaceborne geodetic sensors for hydrology*.
URL: *http://dx.doi.org/10.18419/opus-3929*

Tourian, M. J., Elmi, O., Chen, Q., Devaraju, B., Roohi, S. & Sneeuw, N. (2015), 'A spaceborne multisensor approach to monitor the desiccation of lake urmia in iran', *Remote Sensing of Environment* **156**, 349–360.
URL: *https://doi.org/10.1016/j.rse.2014.10.006*

Tourian, M. J., Elmi, O., Mohammadnejad, A. & Sneeuw, N. (2017), 'Estimating river depth from swot-type observables obtained by satellite altimetry and imagery', *Water* **9**(10), 753.
URL: *https://doi.org/10.3390/w9100753*

Tourian, M. J., Sneeuw, N. & Bárdossy, A. (2013), 'A quantile function approach to discharge estimation from satellite altimetry (envisat)', *Water Resources Research* **49**(7), 4174–4186.
URL: *https://doi.org/10.1002/wrcr.20348*

Uebbing, B., Kusche, J. & Forootan, E. (2015), 'Waveform retracking for improving level estimations from topex/poseidon, jason-1, and jason-2 altimetry observations over african lakes', *IEEE Transactions on Geoscience and Remote Sensing* **53**(4), 2211–2224.
URL: *https://doi.org/10.1109/TGRS.2014.2357893*

Wingham, D., Rapley, C. & Griffiths, H. (1986), New techniques in satellite altimeter tracking systems, *in* 'Proceedings of IGARSS', Vol. 86, pp. 1339–1344.
URL: *http://discovery.ucl.ac.uk/id/eprint/1535543*